scientific reports

Check for updates

OPEN

Application of a two-dimensional phase unwrapping algorithm to lubricant film thickness measurement

Longjun Xie, Zhisong Li✉ & Long Lin

In the precise characterization of microscopic surface morphology, phase unwrapping constitutes a critical step for achieving quantitative reconstruction in interferometric measurements. In lubricating oil-film contact imaging, phase unwrapping algorithms are frequently affected by noise interference, edge blurring, and dynamic operating conditions, which can lead to phase discontinuities and a limited effective unwrapping range. These issues consequently degrade the continuity and accuracy of the reconstructed results. To improve the robustness of phase unwrapping and the accuracy of oil-film thickness reconstruction, this study develops an improved unwrapping method based on the Sorting by Reliability following a Non-Continuous Path (SRNCP) framework for lubricating oil-film interferometric images. By combining phase gradients with local noise estimation to construct a composite quality map and integrating it into the non-continuous path-guided unwrapping process, the proposed method enhances phase unwrapping stability and reconstruction accuracy under complex interferometric conditions. Comparative experiments demonstrate that the improved algorithm achieves significantly enhanced performance in oil film thickness reconstruction compared to traditional methods. Finally, applying the improved unwrapping algorithm to practical lubricating oil film thickness detection further validates its engineering applicability under complex operating conditions.

Keywords Interferometry, Phase unwrapping, Lubricated contact imaging, Improved unwrapping algorithm

With the rapid advancement of intelligent manufacturing, energy systems, and information technologies, human understanding of microstructures, interfacial behaviors, and their dynamic evolution has been continuously extended to higher dimensions, thereby imposing increasingly stringent requirements on the precision, speed, and robustness of interferometric measurement techniques[1]. Owing to its inherent advantages, including high resolution, non-contact operation, and exceptional sensitivity, interferometric metrology based on optical coherence principles has become a cornerstone of multiscale precision measurement systems[2]. In particular, its sub-nanometer thickness resolution has demonstrated significant application potential in a wide range of fields, such as lubricating oil film thickness measurement, precision optical manufacturing, semiconductor device inspection, and high-accuracy surface morphology reconstruction[3,4].

In the aforementioned measurement and imaging systems, phase information constitutes the core of quantitative inversion[5,6]. Phase unwrapping (PU), as a critical step for recovering continuous phase distributions, has been widely employed in a variety of phase measurement and quantitative imaging techniques[7]. Representative applications include phase-shifting interferometry (PSI)[5], Fourier transform interferometry (FTI)[8], and laser speckle interferometry (LSI) in optical interferometric metrology[9]; interferometric synthetic aperture radar (InSAR) in remote sensing and geoscience[10]; as well as magnetic resonance imaging (MRI) in medical imaging[11]. Furthermore, in fringe projection profilometry (FPP) for structured-light three-dimensional measurement, phase unwrapping likewise plays a pivotal role in surface reconstruction[12]. Typical implementations of FPP encompass Fourier transform profilometry (FTP)[13], phase-shifting profilometry (PSP)[14], moiré profilometry (MP)[15], computer-generated moiré profilometry (CGMP)[16], modulation measurement profilometry (MMP)[17], phase-differencing profilometry (PDP)[18], as well as approaches based on empirical mode decomposition (EMD) and related techniques[19]. These cross-disciplinary applications collectively indicate that, under complex conditions such as noise contamination, fringe discontinuities, decorrelation, and large phase gradients, the accuracy and

College of Machine, Shanghai Dianji University, Shanghai 201306, P. R. China. ✉email: song272808216@163.com

robustness of phase unwrapping often directly determine the final inversion quality of key parameters, including thickness, displacement, and surface morphology.

However, owing to the inherent limitations of interferometric imaging mechanisms, the measured phase is typically defined only within a principal value interval of $(-\pi,\pi]$ or $(0,2\pi]$ and exhibits periodic wrapping behavior, leading to the well-known phenomenon of phase wrapping. This characteristic prevents the establishment of a direct and continuous correspondence between the measured phase and the underlying physical quantities. Consequently, phase unwrapping algorithms are required to recover the wrapped phase into a continuous phase distribution with clear physical significance[20,21]. In recent years, to further enhance unwrapping accuracy and robustness under complex imaging conditions, research efforts have primarily advanced along several directions, including spatial-domain strategies, optimization frameworks incorporating prior constraints, and spatiotemporal joint modeling approaches[22,23].

Within the classical framework of spatial phase unwrapping (SPU), quality-map-guided path following remains the most widely adopted technical approach. A variety of quality metrics have been proposed and systematically compared in the literature, and the results indicate that frequency-domain-based quality maps often provide more reliable path guidance in regions with low-quality or severely degraded fringes[22]. Meanwhile, the residue- and branch-cut-based algorithmic family, exemplified by the work of Goldstein et al., has continued to evolve. By incorporating mechanisms such as residue classification, path selection, and network-flow optimization, these methods effectively alleviate the issues of excessively long branch cuts and error accumulation under high-noise conditions, thereby improving phase continuity in locally degraded regions[24]. Furthermore, optimization paradigms combined with prior constraints have been introduced into phase unwrapping models-such as robust loss functions, residue consistency constraints, and global smoothness terms-to mitigate error propagation to a certain extent. Among them, sparse prior-based phase unwrapping (SPUP) achieves a favorable balance between smooth regions and sharp phase discontinuities through L_0/L_1 regularization, demonstrating high fidelity across various phase recovery tasks[23,25]. In addition, iterative models that integrate nonlocal low-rank constraints with the transport of intensity equation have also exhibited strong robustness under severe noise conditions. As interferometric measurement scenarios increasingly evolve toward dynamic and low-coherence regimes, conventional two-dimensional unwrapping strategies encounter limitations in simultaneously preserving temporal continuity and spatial consistency. Consequently, spatiotemporal joint phase unwrapping models have attracted growing research attention[26]. In fields such as InSAR, three-dimensional minimum-cost-flow-based and extended spatiotemporal unwrapping approaches introduce deformation priors along the temporal dimension while incorporating closure-phase constraints in the spatial domain. This formulation elevates phase recovery from a planar solution to a spatiotemporal joint optimization framework, significantly enhancing reliability under challenging conditions including decorrelation, fringe discontinuities, and large phase gradients[27].

In summary, although existing phase unwrapping methods have achieved significant progress in noise suppression and joint modeling, most approaches still rely, to varying degrees, on relatively ideal fringe quality and specific imaging modalities. As a result, their adaptability to common challenges in lubricated contact imaging-such as nonuniform illumination, fringe blurring, and local signal degradation-remains limited. In particular, for microscale oil film thickness measurement, frequent phase discontinuities, locally low signal-to-noise ratios, and pronounced morphology variations induced by force coupling pose substantial challenges. These factors render conventional spatial phase unwrapping algorithms inadequate in terms of path consistency, reliability assessment in degraded regions, and overall engineering generalization capability.

To address the aforementioned issues, this paper proposes an improved phase unwrapping strategy for lubricating oil film interference images based on the SRNCP framework. It should be noted that the contribution lies not in introducing gradient or noise-aware concepts perse, but in developing a composite quality map that integrates phase gradient and local noise characteristics. This map is then incorporated into the discontinuous-path phase-unwrapping process of SRNCP to enhance reliability assessment and path ordering stability in low-quality regions. This approach constructs a composite quality map integrating phase gradient and local noise characteristics, then incorporates it into the discontinuous path phase unwrapping process of SRNCP. This enhances reliability assessment in low-quality regions and path ordering stability, thereby improving phase unwrapping performance and oil film thickness reconstruction capability under complex fringe backgrounds.

Method

To establish a theoretical framework and foundational key technologies for high-precision oil film thickness measurement. First, starting from the fundamental physical mechanisms of interferometric measurement, we elucidate the formation principles of interference fringes and their role in phase information acquisition; Second, an introduction to the principles of phase extraction and phase unwrapping. Building upon this foundation, the SRNCP phase unwrapping algorithm and its improvement strategies are analyzed in detail. An enhanced workflow is proposed, and a calibration mapping between phase and oil film thickness is established. Finally, the improved algorithm is applied to oil film thickness detection under elastohydrodynamic lubrication (EHL) conditions.

Principle of oil-film interferometry

Figure 1(a) illustrates the mechanism of oil-film interference formation in a three-layer structure consisting of a glass disk, an oil film, and a steel ball. When white light is incident on this structure, a portion of the incident light is reflected at the upper interface of the oil film (the glass disk/oil film interface). The remaining light transmits through the oil film, reaches the lower interface (the oil film/steel ball interface), and is reflected again back toward the incident direction. Since these two reflected beams originate from the same incident light, they can be regarded as coherent waves with identical frequencies and a stable phase relationship, thereby satisfying the

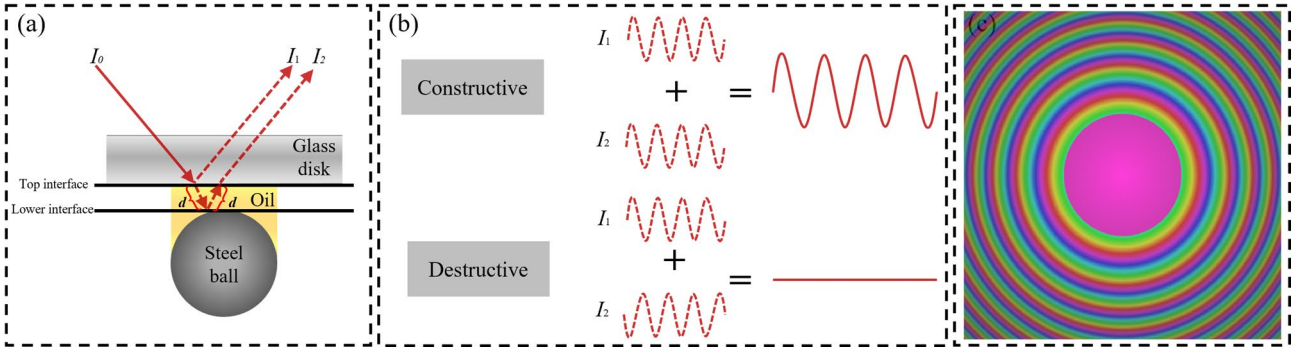

Fig. 1. Formation of oil film interference and its interference patterns: (**a**) Schematic diagram of constructive and destructive interference in two-beam interference; (**b**) Schematic illustration of constructive and destructive interference in two-beam interference; (**c**) Color interference fringes.

conditions for interference. Consequently, when the two reflected beams superpose in the outgoing direction, an interference effect is produced[28].

Due to the different optical paths experienced by the two reflected beams during propagation, an optical path difference ΔL is generated, which correspondingly results in a phase difference $\Delta\varphi$. According to the geometric optics of thin-film interference, the optical path difference mainly arises from the round-trip propagation of the second beam within the oil film, which can be expressed as $\Delta L = 2d$ (where d is the oil-film thickness)[29]. The relationship among the phase difference $\Delta\varphi$, the optical path difference ΔL, and the wavelength λ is given in Eq. (1)[30]:

$$\Delta\varphi = \frac{2\pi}{\lambda} \cdot \Delta L \tag{1}$$

Here, $\Delta\varphi$ represents the phase difference between the two beams, λ denotes the wavelength of the interfering light, and ΔL indicates the optical path difference. In optical interference images, the pixel color is determined by the interference intensity resulting from the superposition of the two coherent beams. The spatial distribution of color reflects variations in the interference intensity I, which is characterized by a cosine relationship with the phase difference $\Delta\varphi$ between the two beams. The interference intensity I is expressed as Eq. (2)[31]:

$$I = I_1 + I_2 + 2\sqrt{I_1 I_2}\cos(\Delta\varphi) \tag{2}$$

Here, I denotes the resultant interference intensity formed by the superposition of the two reflected beams, while I_1 and I_2 represent the reflected intensities from the upper and lower interfaces of the lubricant film, respectively. As illustrated in Fig. 1(b), the variation of the interference intensity I is governed by the phase difference $\Delta\varphi$. When $\Delta\varphi = 2m\pi$ (m is an integer), constructive interference occurs, yielding a maximum interference intensity, which corresponds to the bright fringes in the interferometric image. Conversely, when $\Delta\varphi=(2\ m+1)\pi$, destructive interference takes place, resulting in a minimum interference intensity and giving rise to the dark fringes. These conditions for constructive and destructive interference hold for any single monochromatic wavelength[30].

In practical imaging, white-light illumination is employed. Since white light comprises a continuous broadband spectrum, different wavelength components λ correspond to distinct phase differences $\Delta\varphi$, thereby producing wavelength-dependent interference responses under the same film thickness. The interference contributions of all wavelength components are spectrally superimposed at the detector, ultimately forming a composite interferometric image containing wavelength-dependent information. As shown in Fig. 1(c), the superposition of multi-wavelength interference responses from broadband white light gives rise to a colored interferometric fringe pattern characterized by alternating bright and dark regions[32].

Phase extraction and phase unwrapping of interferometric images

Wrapped phase extraction

Based on the fundamental principle of oil-film interference, the interference image obtained during the actual measurement of the oil film is shown in Fig. 2(a); therefore, the interference intensity can be regarded as known. As indicated by Eq. (2), the superposed interference intensity is only related to the cosine term of the phase difference between the two beams, $\cos(\Delta\varphi)$. However, due to the multivalued nature of the cosine function with respect to the phase difference, identical interference intensities are obtained when $\Delta\varphi$ takes values of $\Delta\varphi$ and $-\Delta\varphi$, or $\Delta\varphi$ and $\Delta\varphi + 2k\pi$ (where k is an integer). Therefore, what is inverted from the interferometric image is not the uniquely determined phase difference $\Delta\varphi$, but rather its wrapped phase $\varphi(i,j)$ in the sense of modulus 2π, whose values are constrained within the interval $(-\pi,\pi]$ or $(0,2\pi]$.

To obtain phase features that can characterize the spatial variation of oil-film thickness, the wrapped phase is first extracted from the color interference images. Considering the imaging characteristics of white-light interference and the requirement for stable dynamic film-thickness measurements under EHL conditions, the hue (H) component in the HSV (Hue-Saturation-Value) color space is selected as a phase surrogate, enabling a

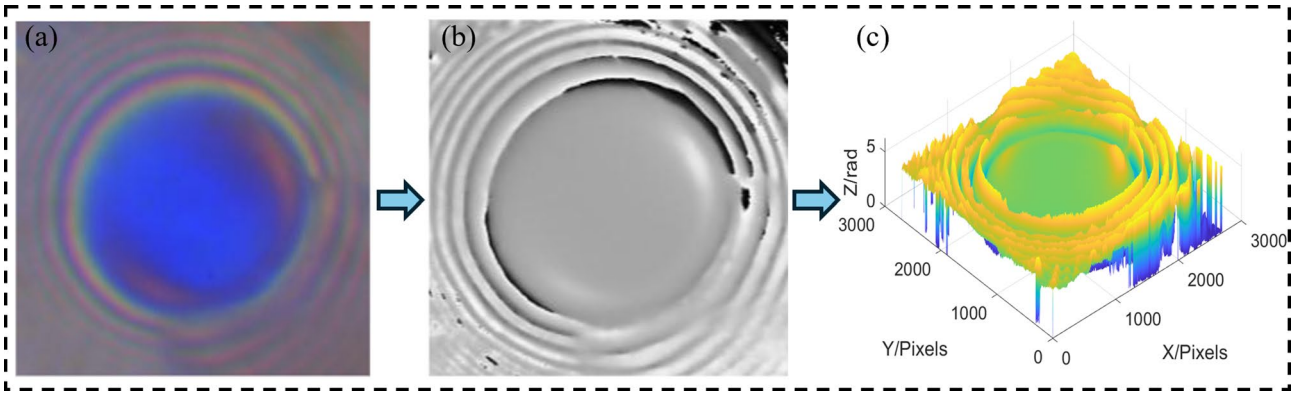

Fig. 2. Flowchart for phase extraction from color interferometric images: (**a**) Color interferometric image; (**b**) Phase feature map of the Hue channel; (**c**) Three-dimensional distribution map of phase wrapping.

robust mapping from color interference images to wrapped phase features. Compared with direct processing of the three RGB intensity channels, the HSV color space effectively decouples color information from luminance information. Specifically, the hue component primarily reflects variations in the dominant wavelength (color), whereas the saturation and value components are more susceptible to illumination nonuniformity, shadowing effects, and camera gain drift. Therefore, under white-light interference conditions, the use of the hue component is more effective in suppressing intensity disturbances and enhancing the robustness of phase feature extraction. Based on this concept, the color interference image is first converted from the RGB space to the HSV space, and the hue channel is extracted to obtain the hue-based phase feature grayscale image, as shown in Fig. 2(b).

The method of phase characterization based on the hue component in thin-film interference has been systematically investigated and reported in the existing literature[33,34]. For the convenience of subsequent algorithm implementation and performance evaluation, this section only presents the mathematical definitions and key implementation aspects that are directly related to phase acquisition. First, for the color interference images after linearized acquisition, white-balance correction, and dark-field correction, the intensities of the three channels are denoted as $(R,G,B)\in[0,1]$. The image is then mapped into the HSV color space. In the calculation of the hue component, a four-quadrant inverse tangent function is employed to obtain a continuous angular representation, which is defined as shown in Eq. (3):

$$H = \arctan 2\left(\frac{2G - R - B}{R - B}\right) \tag{3}$$

Here, arctan2(·) denotes the four-quadrant inverse tangent function; G represents the green channel, R the red channel, and B the blue channel. The use of the four-quadrant inverse tangent ensures that correct angular quadrant information is preserved when crossing the boundary at $(0,2\pi)$, thereby avoiding nonphysical phase jumps and numerical discontinuities caused by branch switching of the conventional arctangent function.

It should be noted that the hue component is intrinsically an angular quantity modulo 2π; therefore, its spatial distribution naturally exhibits wrapped phase characteristics. When the angle crosses the $(0,2\pi)$ boundary, the numerical value abruptly jumps from the maximum to the minimum, or vice versa. Such spatial discontinuities are mathematically consistent with the two-dimensional phase unwrapping problem. Accordingly, the hue component can be regarded as a wrapped phase signal, from which a continuous phase distribution can be recovered through subsequent two-dimensional phase unwrapping. For the convenience of data storage and visualization, the hue values are normalized to the range [0,1]; however, during phase computation and unwrapping, they are still processed in radians, with the interval [0,1] mapped back to $(0,2\pi)$ to preserve phase-topological consistency. The final wrapped phase result is shown in Fig. 2(c), which presents the three-dimensional distribution of the wrapped phase obtained from the color interference image via hue-channel extraction. This result fully illustrates the phase extraction workflow, progressing from the color interference image in Fig. 2(a), to the hue-based phase feature map in Fig. 2(b), and finally to the three-dimensional wrapped phase distribution in Fig. 2(c).

Phase unwrapping

Figure 3(a) shows the wrapped phase map. Although the wrapped phase can reflect local phase variations, it cannot describe the globally continuous phase and therefore cannot be directly used for surface profile reconstruction. To obtain a continuous oil-film thickness distribution, the wrapped phase must be converted into a continuous phase[20,21]. Figure 3(b) presents the corresponding continuous phase distribution. The transformation relationship from the wrapped phase to the continuous phase is given by Eq. (4)[20]:

$$\phi(i,j) = \varphi(i,j) + 2\pi \cdot k(i,j) \tag{4}$$

Here, $\phi(i,j)$ denotes the unwrapped phase, which reflects the actual physical quantity of interest. $\varphi(i,j)$ represents the wrapped phase extracted from the interferometric image and is confined to the principal interval $(0,2\pi]$.

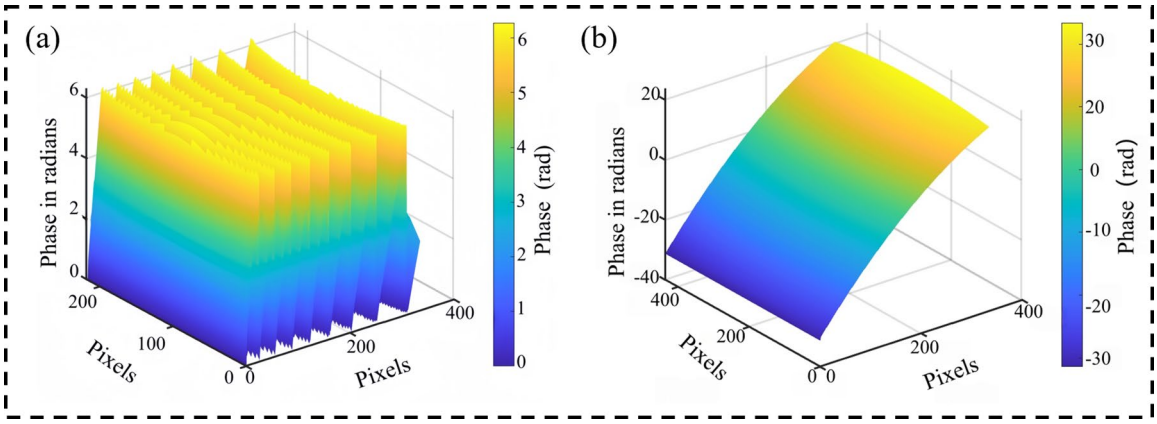

Fig. 3. Illustration of phase wrapping and continuous phase: (**a**) Schematic of phase wrapping; (**b**) Schematic of continuous phase.

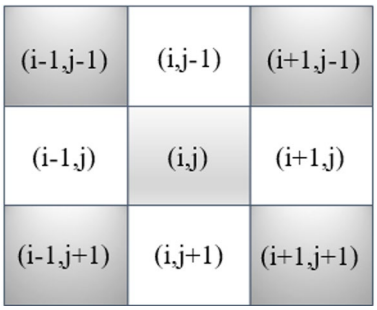

Fig. 4. 3 × 3 Pixel neighborhood structure diagram.

The integer-valued function $k(i,j)$ indicates the cumulative number of 2π phase jumps accumulated along the unwrapping path from a reference point to the location (i,j).

Principle of the SRNCP phase unwrapping algorithm

The SRNCP algorithm is a classic two-dimensional phase unwrapping method. Its core principle involves constructing a quality map to evaluate the credibility of each pixel's phase structure. Based on this quality map, edge reliability values are calculated and ranked, enabling gradual phase unwrapping along the optimal discontinuous path. The processing flow of the SRNCP algorithm can be described as follows: Starting from the original wrapped phase, a reliability quality map is constructed by calculating phase gradients and second-order differences. A global priority sorting is then performed based on edge reliability. Subsequently, phase unwrapping is implemented along the optimal discontinuous path to obtain a continuous phase distribution with global consistency. The algorithm primarily consists of two core steps in its processing flow: constructing the reliability quality map and performing discontinuous path unwrapping[7].

Constructing a reliability quality map

The construction of a reliability quality map involves three steps: calculating phase gradient magnitudes, computing second-order differences, and generating the final quality map based on these second-order differences. By following these steps, the robustness of local phase structures can be effectively evaluated, thereby providing reliable guidance for the phase unwrapping process[7]. Taking a 3 × 3 neighborhood structure as an example, as shown in Fig. 4.

First, the magnitude of the phase gradient between adjacent pixels is calculated to assess the smoothness of local phase variations. To this end, horizontal and vertical gradients are defined to quantitatively describe the rate of phase change within local regions[7]. The horizontal gradient is expressed in Eq. (5), while the vertical gradient is given in Eq. (6).

$$H(i,j) = \gamma\left[\varphi(i-1,j) - \varphi(i,j)\right] - \gamma\left[\varphi(i,j) - \varphi(i+1,j)\right] \tag{5}$$

$$V(i,j) = \gamma\left[\varphi(i,j-1) - \varphi(i,j)\right] - \gamma\left[\varphi(i,j) - \varphi(i,j+1)\right] \tag{6}$$

Here, $\gamma(\xi)$ is the normalizing function that maps any phase value ξ to the principal interval (-π,π]. $\varphi(\xi)$ denotes the reflected phase obtained from the interference image, corresponding to the measured phase difference $\Delta\varphi$.

After obtaining the phase gradient, to further characterize the smoothness of local phase variations, the gradients in the horizontal, vertical, and diagonal directions are combined to compute a second-order difference. This enhances sensitivity to changes in local phase structure. Consequently, the computational form of the second-order difference is expressed as shown in Eq. (7):

$$D(i,j) = \left[H^2(i,j) + V^2(i,j) + {D_1}^2(i,j) + {D_2}^2(i,j)\right]^{\frac{1}{2}} \tag{7}$$

Here, the diagonal directional difference is shown in Eqs. (8) and (9)[7]:

$$D_1(i,j) = \gamma\left[\varphi(i-1,j-1) - \varphi(i,j)\right] - \gamma\left[\varphi(i,j) - \varphi(i+1,j+1)\right] \tag{8}$$

$$D_2(i,j) = \gamma\left[\varphi(i-1,j+1) - \varphi(i,j)\right] - \gamma\left[\varphi(i,j) - \varphi(i+1,j-1)\right] \tag{9}$$

Based on the local second-order difference value $D(i,j)$, its reciprocal is taken as the evaluation criterion to construct a reliability quality map, thereby obtaining the reliability distribution of pixels[7]. The reliability is expressed as shown in Eq. (10):

$$R(i,j) = \frac{1}{D(i,j)} \tag{10}$$

Here, $D(i,j)$ represents the second-order difference value. A higher reliability value $R(i,j)$ indicates smoother and more reliable local phase, whereas a lower reliability value suggests that the region is more susceptible to noise or edge abrupt changes.

Non-contiguous path phase unwrapping

Assume the quality map obtained by calculating reliability is shown in Fig. 5(a), which is used to evaluate the reliability of each pixel. The SRNCP algorithm constructs paths based on edge reliability values, as illustrated in Fig. 5(b). Each pair of adjacent pixels in the image is connected by an edge, primarily comprising horizontal (light orange) and vertical (blue) edges. The reliability of each edge is defined as the sum of the reliability values of its two end pixels. This approach constructs a reliability array encompassing all edges. Subsequently, all edge reliability arrays are sorted in descending order by magnitude. Pixel pairs connected by high-reliability edges are prioritized, progressively constructing multiple non-overlapping connected regions. This path strategy, which gradually expands from high-quality to low-quality regions, effectively suppresses error propagation caused by low-credibility areas (such as noise and jump points), significantly enhancing the overall robustness and accuracy of unwrapping[7].

The SRNCP algorithm achieves path search by constructing local connectivity relationships during phase unwrapping, making it highly sensitive to the accuracy of reliability evaluation. When images exhibit edge blurring, localized high noise, or pronounced phase discontinuities, reliability metrics based on edge consistency may yield biased results, thereby compromising the stability of pixel grouping and path ordering.

Principles of the improved phase unwrapping algorithm

To enhance the adaptability and robustness of the SRNCP algorithm under complex interference image conditions, this paper addresses the issue of reliability assessment distortion under local fringe degradation and noise contamination by improving the original reliability quality map. Specifically, this paper constructs a composite reliability representation by integrating local phase gradient and noise estimation information. This representation is then incorporated into the discontinuous path phase unwrapping framework of SRNCP to enhance path guidance stability and phase unwrapping consistency in complex interferometric images[35,36].

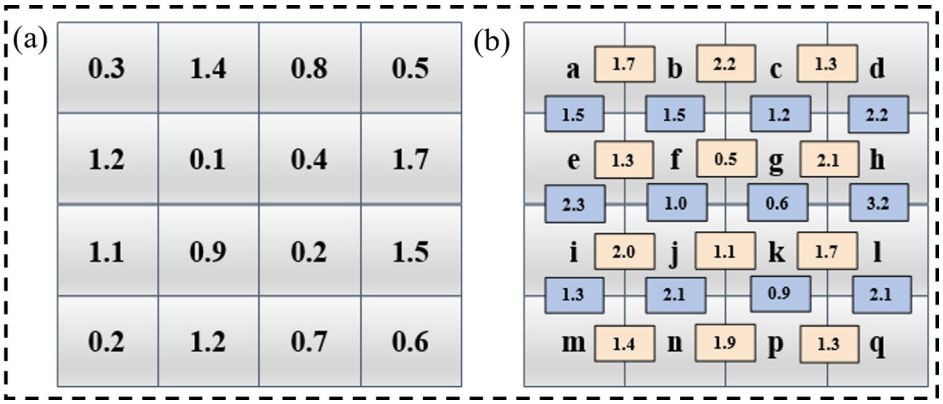

Fig. 5. Pixel and edge reliability ranking: (**a**) Pixel reliability ranking; (**b**) Edge reliability ranking.

Adaptive noise-weighted reliability function

In traditional SRNCP algorithms, reliability is estimated based on local phase gradient variations. However, in actual interferometric images, gradient changes originate not only from genuine phase jumps but are also affected by noise perturbations. Based on this, this paper constructs a quality factor that jointly weights local noise levels and phase gradients[37], as shown in Eq. (11). This design does not aim to propose a novel theoretical model independent of existing quality map concepts. Instead, it enhances the reliability assessment within SRNCP by incorporating locally degraded features commonly observed in EHL interference images, thereby tailoring the approach to specific application scenarios.

It should be noted that a 3 × 3 neighborhood structure is adopted for local noise estimation in this paper. This setting maintains consistency with the neighborhood scale used in the original SRNCP reliability assessment, ensuring uniformity between the improved strategy and the original method at the local analysis scale. Furthermore, the 3 × 3 neighborhood strikes a balance between locality constraints and noise statistical stability. It avoids excessive smoothing of edges and phase jump regions caused by overly large neighborhoods while providing relatively stable local statistical features, thereby more reasonably characterizing the noise level within the pixel neighborhood.

$$Q(i,j) = g(i,j) \cdot \alpha(i,j) \tag{11}$$

Here, $g(i,j)$ denotes the magnitude of the phase gradient, while $\alpha(i,j)$ represents the local noise intensity adjustment coefficient. The phase gradient is composed of horizontal and vertical components, as shown in Eq. (12):

$$g(i,j) = \left[\left(\frac{\partial \varphi}{\partial x} \right)^2 + \left(\frac{\partial \varphi}{\partial y} \right)^2 \right]^{\frac{1}{2}} \tag{12}$$

Here, $\partial\varphi/\partial x$ and $\partial\varphi/\partial y$ represent the phase gradient variation magnitudes in the horizontal and vertical directions, respectively, used to quantify the degree of local phase changes. To characterize local texture perturbations and noise intensity, this paper employs a 3 × 3 neighborhood structure (as shown in Fig. 4) and calculates the standard deviation as the noise estimation value. The local standard deviation $\sigma(i,j)$ is defined as shown in Eq. (13):

$$\sigma(i,j) = \left[\frac{1}{N} \sum_{k=1}^{N} (I_k - \bar{Y}) \right]^{\frac{1}{2}} \tag{13}$$

Here, I_k denotes the kth pixel value within the 3 × 3 neighborhood centered at pixel (i,j). $\overline{Y}$ represents the average of all I_k values within the 3 × 3 neighborhood, and N denotes the total number of pixels in the neighborhood (for a 3 × 3 window, $N = 9$). Subsequently, the local noise estimate undergoes normalization to obtain the noise suppression factor $\alpha(i,j)$, as shown in Eq. (14):

$$\alpha(i,j) = 1 - \frac{\sigma(i,j)}{\max(\sigma)} \tag{14}$$

Here, max(σ) denotes the maximum value of all local mean squares. After normalization, the values of $\alpha(i,j)$ are constrained within the range [0,1], where higher values indicate lower local noise levels and higher reliability of the corresponding pixels. It also facilitates consistent integration with gradient terms and enhances the comparability of reliability modulation under different imaging conditions.

In summary, this paper proposes an improved reliability function that simultaneously considers phase gradient magnitude and local noise intensity, enabling more accurate assessment of pixel phase credibility. The reliability function is expressed as shown in Eq. (15):

$$R(i,j) = \frac{1}{D(i,j)} \cdot Q(i,j) \tag{15}$$

Here, $D(i,j)$ denotes the second-order difference value at pixel location (i,j).

Overall process for improving the algorithm

First, extract the hue channel from the interferometric image to obtain an initial wrapped phase map. Next, calculate the raw edge reliability and reweight it using a noise estimation factor. Sort the reweighted edge reliability array and iteratively connect pixel groups to construct more robust phase unwrapping paths. Ultimately, the algorithm performs phase unwrapping along these highly reliable and discontinuous paths, yielding a continuous phase map that provides precise input for the quantitative reconstruction of lubricant film thickness. The overall workflow of the improved algorithm is illustrated in Fig. 6.

Phase-to-film-thickness mapping

After obtaining the unwrapped continuous phase distribution, it is necessary to convert the phase value of each pixel into the corresponding lubricating oil film thickness, thereby enabling quantitative analysis of the interference image. According to classical interference theory, the relationship between phase and oil-film thickness is given by Eq. (16)[38]:

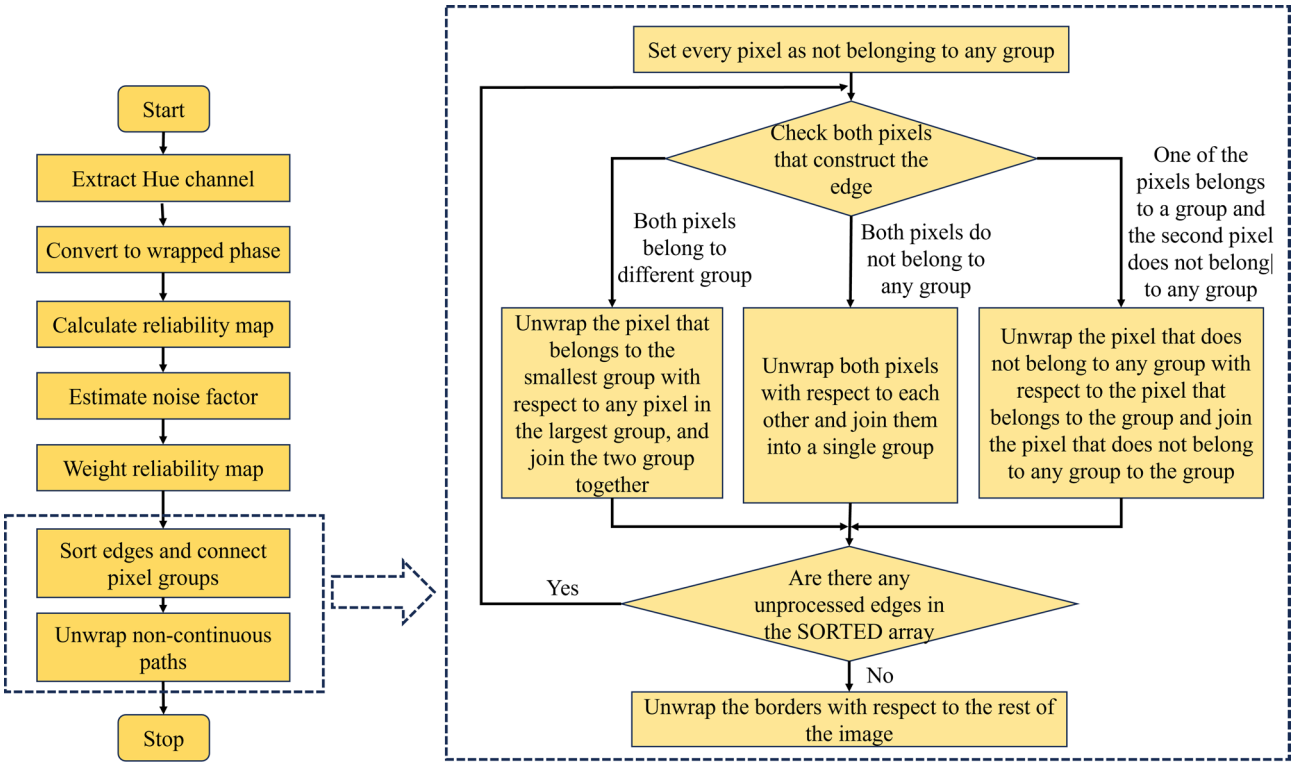

Fig. 6. Overall Flowchart for Algorithm Improvement.

$$h(i,j) = \frac{\lambda}{4\pi n} \cdot \phi(i,j) + h_0 \tag{16}$$

Here, λ denotes the central wavelength of the interference light source, n represents the refractive index of the medium, $\phi(i,j)$ signifies the unfolded phase at the pixel location, and h_0 indicates the thickness zero-point offset used to calibrate the relative phase thickness against the actual geometric thickness of the contact interface.

To obtain absolute oil film thickness information, it is necessary to further utilize Hertzian contact theory to establish an elastic contact model between the steel ball and glass disc. This model describes the theoretical film thickness distribution at any radial position r, as shown in Eq. (17)[39]:

$$h = \frac{r^2}{2R} - \frac{\pi a}{2E^*} + \frac{p_0}{2aE^*}\left[\left(2a^2 - r^2\right)\sin^{-1}\left(\frac{a}{r}\right) + r^2\left(\frac{a}{r}\right)\right]\sqrt{1 + \left(\frac{a}{r}\right)^2} \tag{17}$$

Here, r denotes the radial distance from the contact center point, R represents the curvature radius of the steel ball, a indicates the contact radius, E^* signifies the equivalent elastic modulus, and P_0 denotes the Hertzian contact peak pressure.

In this study, the theoretical gap height at the contact center can be precisely calculated using the Hertzian contact theory model Eq. (16). The maximum phase in the contact center region is selected as the reference phase point. Using Eq. (17), the gap height at this point is determined to obtain the true thickness at the contact center. Subsequently, this true thickness is compared with the thickness calculated at the same position using Eq. (16). The offset h_0 of the thickness zero point is then determined by back-calculation. After calibrating h_0 substituting it into Eq. (16), accurately converts the two-dimensional phase field into a three-dimensional oil film thickness field. Based on the calibrated oil film thickness distribution, a reliable quantitative foundation is provided for lubrication state identification, contact performance evaluation, and surface functionality analysis.

Calculation process and implementation for high-precision extraction of EHL oil film thickness

To achieve high-precision extraction of EHL oil film thickness, this paper proposes a comprehensive measurement workflow illustrated in Fig. 7. First, an interferometric image is acquired, and its Hue channel is extracted as the carrier of modulated phase information. This hue image is then converted into an initial phase envelope map. An improved algorithm processes the phase envelope map to obtain continuous phase data. Finally, the thickness zero-point offset h_0 is calculated based on the Hertzian contact theory model. Using this as a reference, the unwrapped phase map is precisely converted into the lubricant film thickness distribution, enabling the accurate reconstruction of the EHL oil film profile within the contact region.

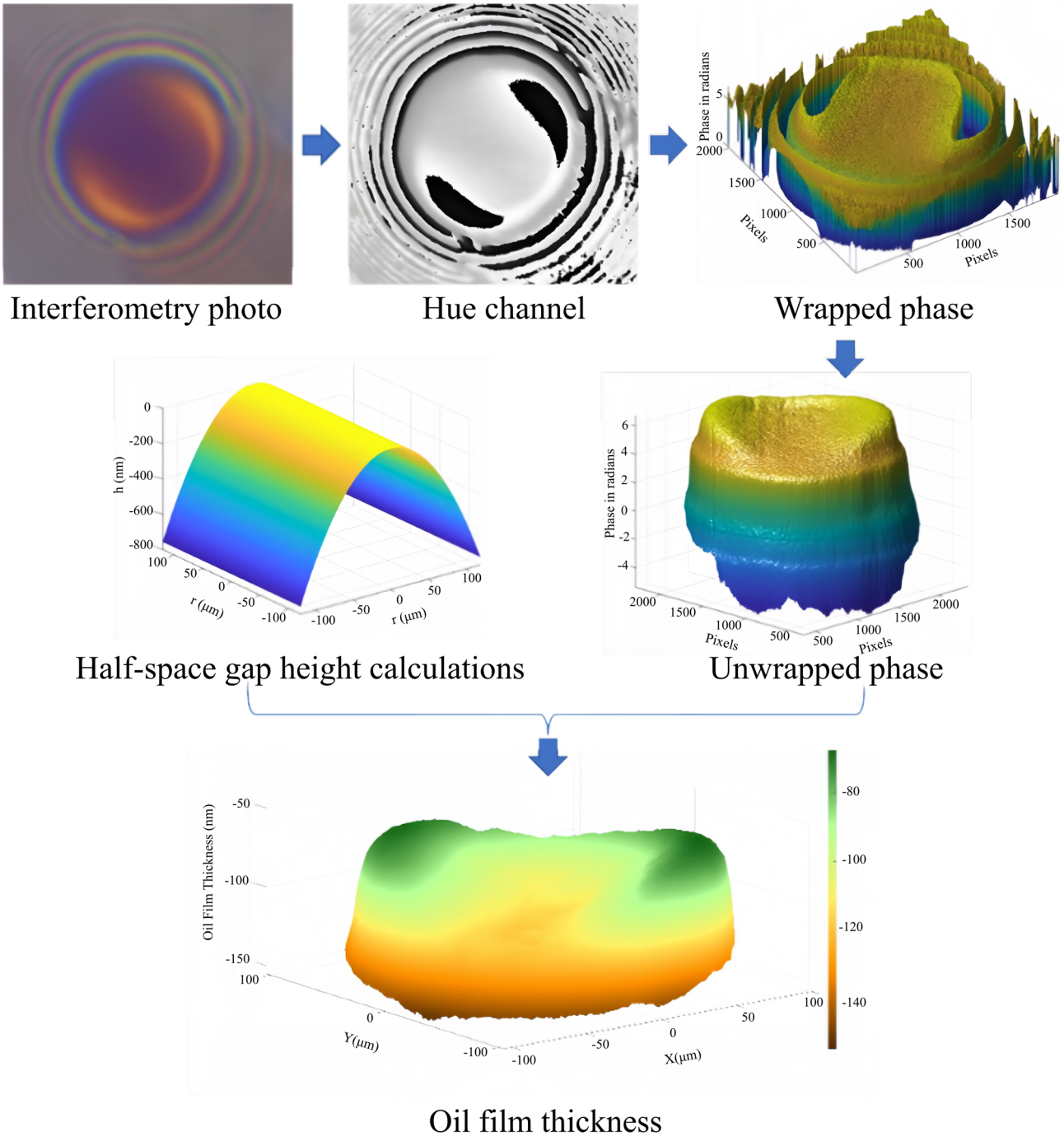

Fig. 7. Flowchart for calculating EHL oil film thickness distribution using an improved algorithm.

Experimental apparatus

All interferometric images used in this study were acquired using a self-built microscopic interferometry platform. The overall system structure is shown in Fig. 8, while a schematic of the experimental setup is depicted in Fig. 9. This platform primarily consists of a broadband white light source, a long-working-distance microscope, a CMOS industrial camera, a controllable loading steel ball-glass plate contact structure, and a computer system for image acquisition and post-processing. It provides the essential hardware foundation for subsequent acquisition and analysis of EHL oil film interferometric images.

The experiment employs a typical elastic point contact structure consisting of a steel ball and a glass plate. By applying static or dynamic normal loads between the two contact bodies via a loading device, a stable lubrication state is established, maintaining a thin oil film between their surfaces. This experimental configuration can effectively reproduce the operating conditions of an EHL oil film, providing reliable conditions for oil-film thickness measurement. The geometric and material parameters of the two contacting bodies are listed in Table 1.

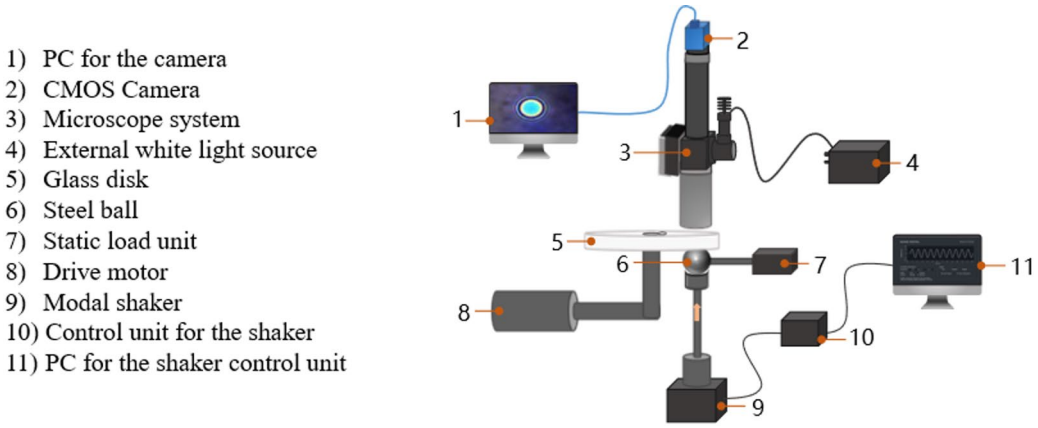

Fig. 8. EHL oil film thickness measurement system design drawing.

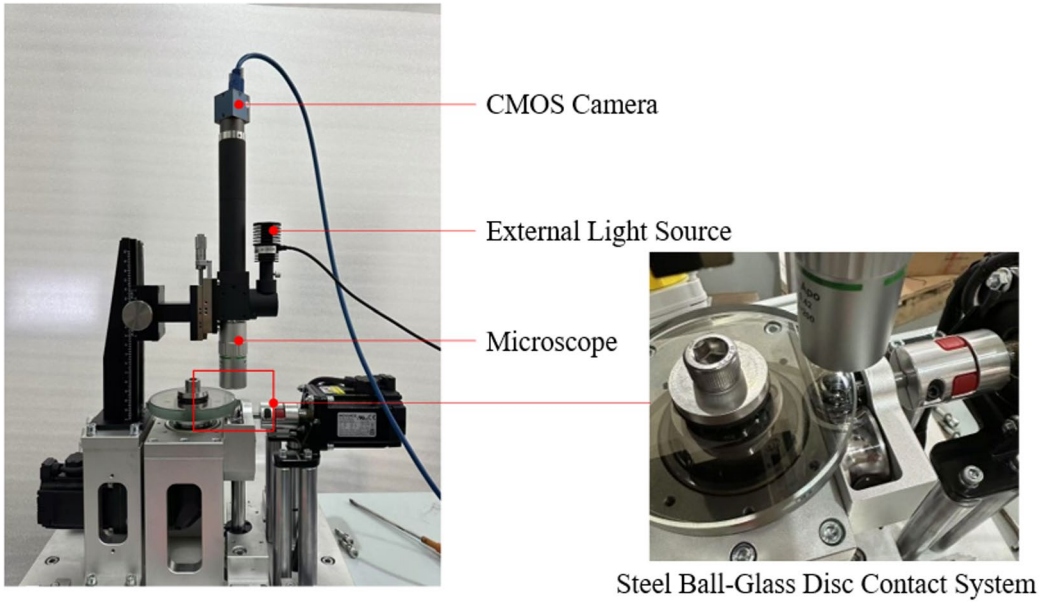

Fig. 9. EHL oil film thickness measurement system experimental setup diagram.

Geometric and material parameters	Contact body 1 (Steel Ball)	Contact body 2 (glass disk)
Geometry	Radius = 9.525 mm	Flat
Elastic Modulus [GPa]	205	74
Poisson's Ratio	0.28	0.21

Table 1. Geometric and material parameters table for steel ball and glass disc contact elements.

Experiment

To comprehensively validate the effectiveness and applicability of the improved phase unwrapping algorithm proposed in this paper for measuring EHL oil film thickness, this chapter establishes a systematic testing plan across different experimental scenarios. Specifically, it includes: phase reconstruction comparison experiments of interferometric images under simulated conditions; phase reconstruction comparison experiments of interferometric images under actual conditions; comprehensive validation experiments on oil film thickness reconstruction accuracy; and application experiments of the improved phase unwrapping algorithm in EHL oil film thickness measurement.

In various experiments, this chapter selects representative phase unwrapping methods, including the Branch-Cut method by Goldstein et al.[40], the Transport of Intensity Equation (TIE)-based algorithm[41], the network-flow (N-F)-based phase unwrapping method introduced by Costantini[24], and the edge reliability-guided SRNCP

Item	Configuration
CPU	Intel® Core™ i7-12700 K @ 3.60 GHz (12 C/20T)
Memory	32 GB DDR4
OS	Windows 11
MATLAB	MATLAB R2023b

Table 2. Runtime testing environment.

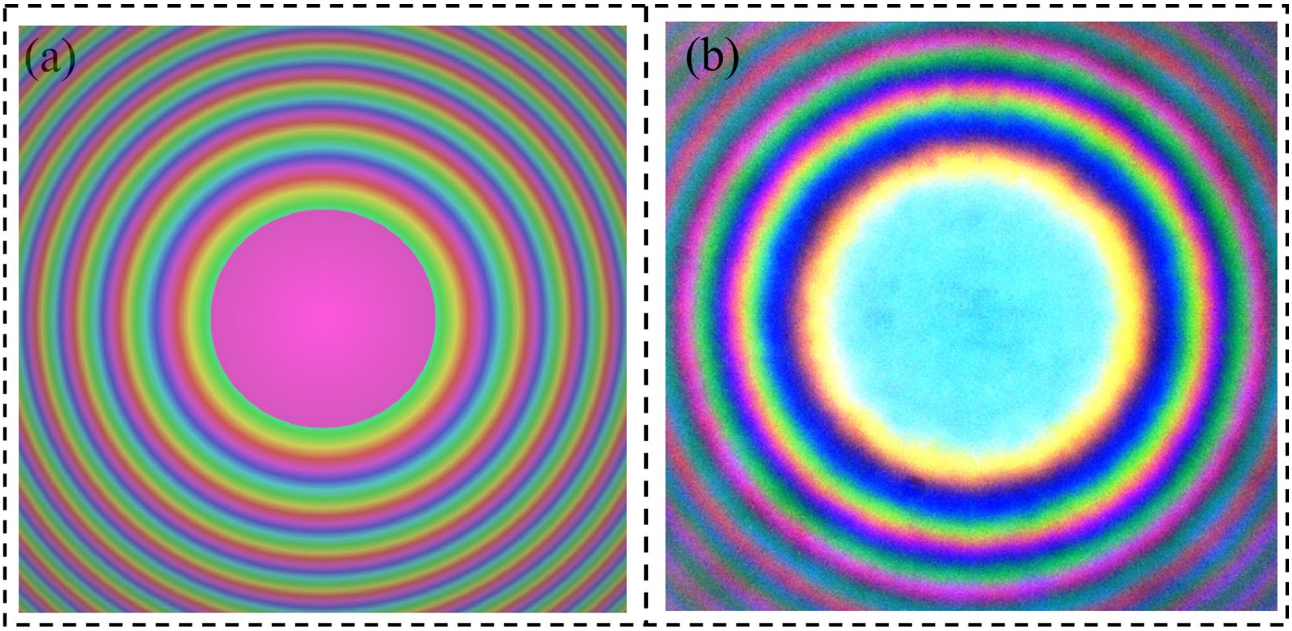

Fig. 10. Simulated and actual interference patterns: (**a**) Simulated interferogram; (**b**) Actual interference pattern.

algorithm[7]. These methods represent different phase-unwrapping strategies rather than algorithms requiring specific tunable parameter configurations. Their implementations mainly follow the algorithmic procedures described in the original references. The detailed algorithmic descriptions and parameter settings can be found in the corresponding literature. These methods are systematically evaluated and compared with the improved algorithm proposed in this chapter.

Computational efficiency evaluation

Computational efficiency serves as a key metric for evaluating the engineering applicability of phase unwrapping algorithms. To ensure a fair comparison of computational performance across different algorithms, this section tests each algorithm under identical hardware and software configurations, as detailed in Table 2:

To comprehensively evaluate the computational efficiency of different algorithms under varying interferometric conditions, simulated and real interferograms were selected as test data, as shown in Fig. 10. Figure 10(a) depicts a simulated interferogram with regular and continuous fringe patterns; Fig. 10(b) presents an actual acquired interferometric image, incorporating real-world measurement characteristics such as noise and intensity inhomogeneity, thereby more closely approximating real-world engineering scenarios. Both images are high-resolution interferometric images with a resolution of 4k×4k pixels.

The runtime statistics for different algorithms are shown in Fig. 11, where Fig. 11(a) depicts the runtime distribution under simulated interferometric data, and Fig. 11 (b) shows the runtime distribution under actual interferometric data. As evidenced by Fig. 11, the proposed improved algorithm demonstrates superior computational efficiency under both data conditions. On simulated data, its average runtime is approximately 6.351 s; on actual interferometric data, the average runtime is approximately 6.314 s, both significantly lower than the traditional algorithm.

Comparative analysis of phase reconstruction in interference images under simulated conditions

To evaluate the robustness of various phase unwrapping algorithms under localized strong-interference conditions, this section constructs a synthetic lubricating oil film interferogram with a resolution of 1024×1024 pixels. Considering that practical interferometric measurements are often affected by local fringe degradation, noise contamination, and reduced phase continuity, Gaussian noise was deliberately introduced into a 200×200

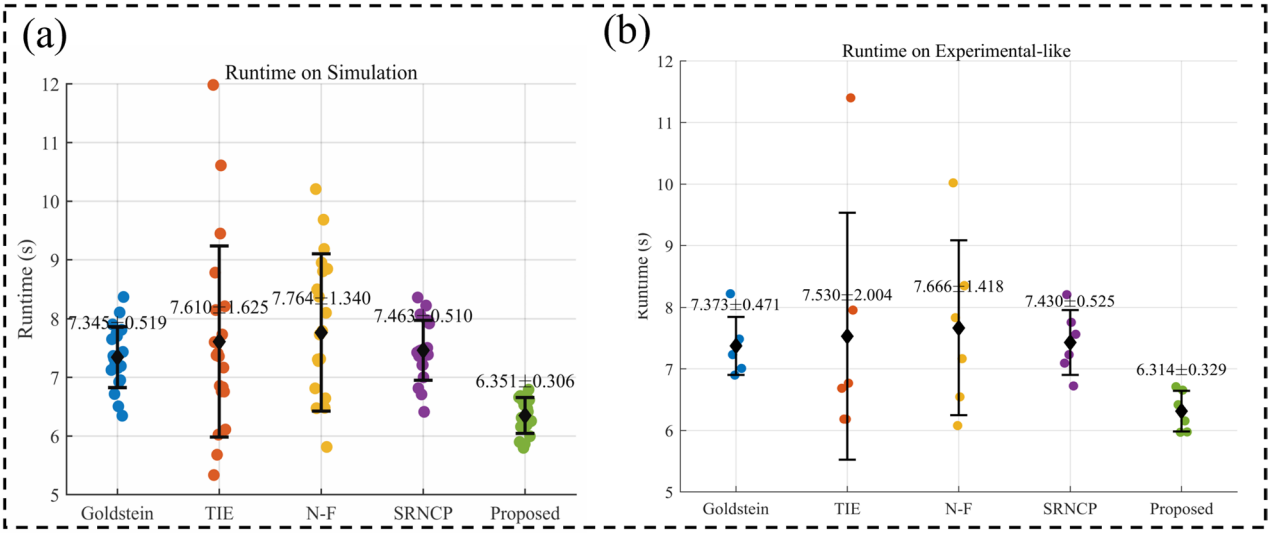

Fig. 11. Runtime of different algorithms on simulated and experimental data: (**a**) Runtime on simulation; (**b**) Runtime on experimental-like.

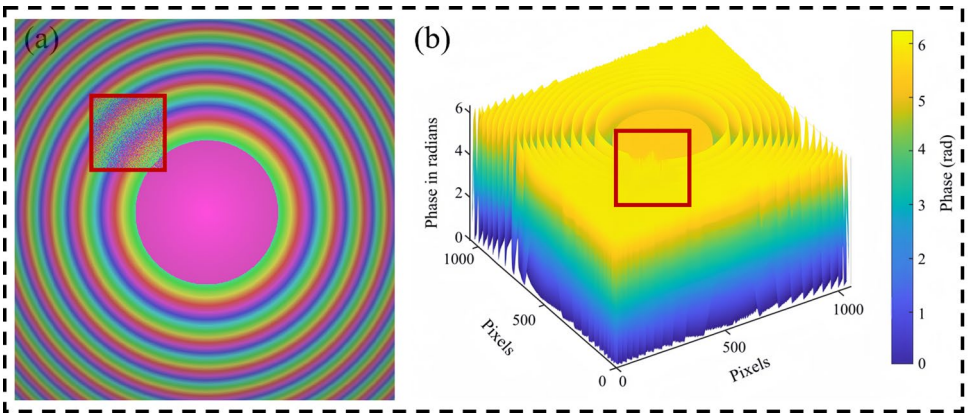

Fig. 12. Simulated interference image and corresponding wrapped phase map: (**a**) Simulated interferogram; (**b**) Phase envelope diagram.

pixel region in the upper-left corner to create a representative locally degraded scenario, as shown in Fig. 12(a). The noise standard deviation was set to 0.8 rad so as to generate a sufficiently strong perturbation capable of markedly disrupting the continuity of the wrapped phase and the reliability ordering, thereby providing a stringent test for comparing the anti-interference performance of different algorithms in adverse local regions. It should be noted that this noise level was not intended to represent a precisely calibrated physical noise condition for a specific experimental case, but rather to serve as a representative strong-noise stress-testing parameter for emulating severe local degradation that may occur in real interferometric images. The corresponding unwrapped phase distribution is shown in Fig. 12(b), which serves as the baseline input for the subsequent comparative evaluation of algorithm performance.

Figure 13 presents a visual comparison of three-dimensional phase reconstruction results from five representative phase unwrapping algorithms: Goldstein et al.'s branch-cutting method, the TIE algorithm, the N-F algorithm, the SRNCP algorithm, and the improved algorithm proposed in this paper. Figure 13(e1) and Fig. 13(e2) specifically demonstrate the reconstruction achieved by the improved algorithm. As evident from the figure, even when affected regions exhibit strong noise interference, the improved algorithm successfully restores a smooth and continuous phase surface overall, fully demonstrating its robustness and stability under locally degraded conditions. To better visualize local recovery differences under strong noise, we further provide zoom-in views of the contaminated region in Fig. 13.

The quantitative comparison results are presented in Table 3. For all evaluation metrics, lower values correspond to better performance. Among them, the Gradient Magnitude Similarity Deviation (GMSD)[42], quantifies the local gradient deviation of the reconstructed phase map, thereby reflecting phase continuity, smoothness, and local distortion. The proposed method achieves the lowest GMSD, indicating superior phase

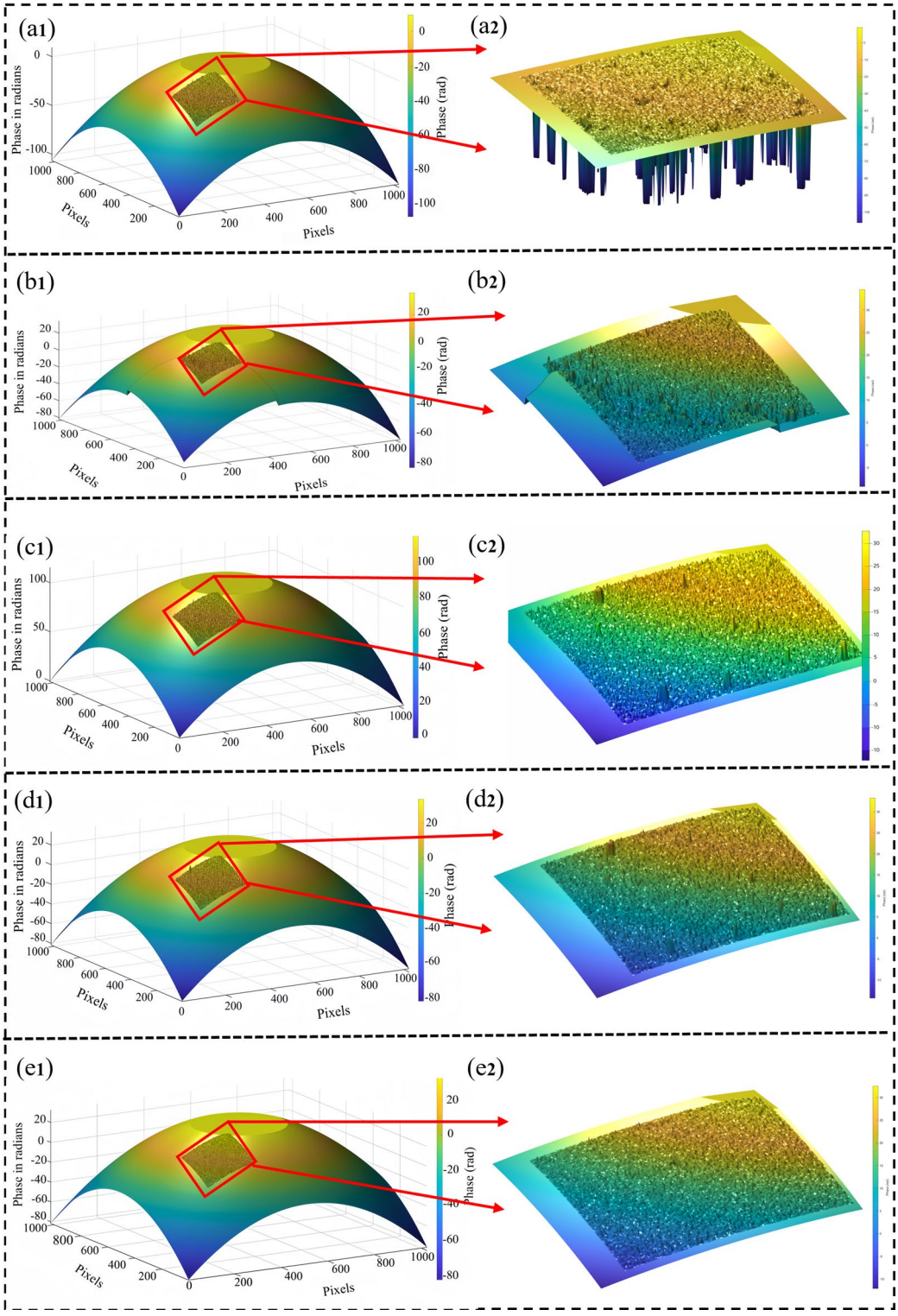

Fig. 13. Five phase unwrapping algorithms for 3D reconstruction of noised phase maps: (a1) Goldstein algorithm (global 3D phase surface); (a2) Goldstein algorithm (local enlarged 3D reconstruction). (b1) TIE algorithm (global 3D phase surface); (b2) TIE algorithm (local enlarged 3D reconstruction). (c1) N-F algorithm (global 3D phase surface); (c2) N-F algorithm (local enlarged 3D reconstruction). (d1) SRNCP algorithm (global 3D phase surface); (d2) SRNCP algorithm (local enlarged 3D reconstruction). (e1) Improved algorithm (global 3D phase surface); (e2) Improved algorithm (local enlarged 3D reconstruction).

Algorithm	Phase smoothness (GMSD)	Unwrapping errors in noisy region (pixel)	Noise sensitivity (local gradient Std. Dev.)
Goldstein Method	3.0579	4466	1.4948
TIE Method	0.2299	2677	0.6993
N-F Method	0.1796	1320	0.4850
SRNCP Method	0.1579	600	0.4503
Improved Method	0.1177	25	0.2894

Table 3. Quantitative performance comparison of five phase-unwrapping algorithms across different evaluation metrics.

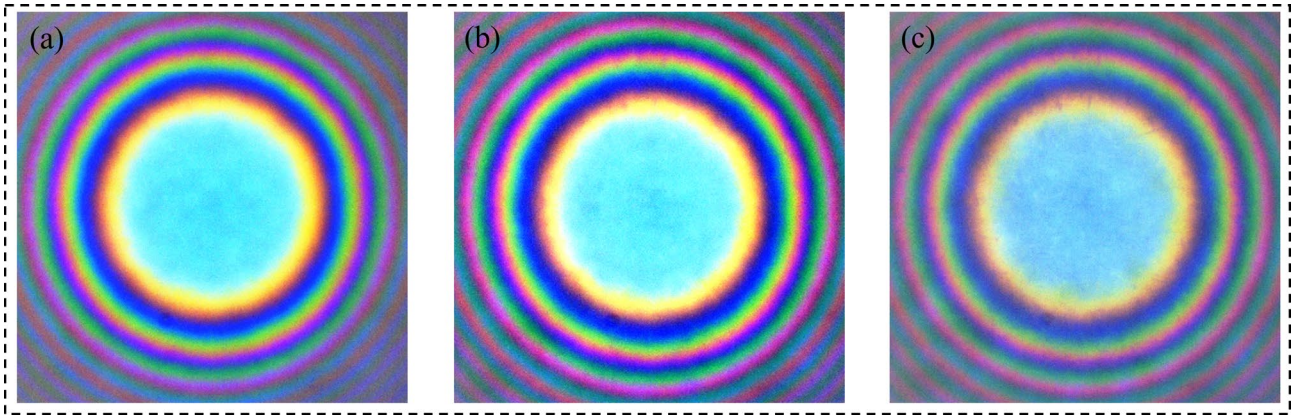

Fig. 14. Acquire three consecutive frames of transient interference images: (**a**) First frame; (**b**) Second frame; (**c**) Third frame.

smoothness and reconstruction quality. The metric of unwrapping errors in noisy regions counts the number of incorrectly unwrapped pixels and is used to evaluate robustness under severe noise interference. In this respect, the improved algorithm yields only 25 phase-jump errors, significantly outperforming the competing methods. Moreover, noise sensitivity, measured by the local gradient standard deviation, characterizes the fluctuation of local phase gradients; a lower value indicates weaker noise sensitivity and better local stability. The proposed method again achieves the best result, demonstrating clear advantages over existing methods in both reconstruction accuracy and stability.

Comparative analysis of phase reconstruction in interference images under actual operating conditions

To comprehensively evaluate the effectiveness and robustness of the improved phase unwrapping algorithm under practical operating conditions, this section designed a comparative experiment for phase reconstruction of transient interferometric images. In the experimental setup, a glass disc and steel ball rotated synchronously at 10 r/min while subjected to an external load of 1 N. The ambient temperature was maintained at a constant 20 °C. A high-resolution transient interferometric image with a resolution of 2000×2000 pixels was captured using a microscopic interferometry system. Figure 14 displays three consecutive frames of transient interferometric images.

Phase unwrapping is performed separately on the three transient interference images, and the reconstruction results of the five algorithms are systematically compared. Figure 15 shows the reconstructed phase distributions obtained by each algorithm for the three frames. By comparing the performance of different algorithms in terms of effective unwrapping area, phase smoothness, and the number of error regions, the applicability and performance advantages of the improved algorithm under complex interference-fringe conditions can be further verified.

According to the quantitative results of the three-frame interferometric images under the five phase unwrapping algorithms presented in Table 4, clear differences can be observed among the methods in terms of effective unwrapped area, phase smoothness, and the number of unwrapping error regions. Overall, the improved algorithm achieves the best performance across all experimental frames, demonstrating excellent robustness and stability.

Specifically, the effective unwrapped area represents the ratio of successfully recovered continuous phase area and reflects the valid coverage of phase reconstruction in complex or degraded regions; for this metric, higher values indicate better performance. The improved algorithm attains coverage rates of 98.642%, 98.906%, and 98.951% for the three frames, respectively, which are the highest among the five methods, indicating its superior unwrapping capability even under complex phase structures and strong noise interference.

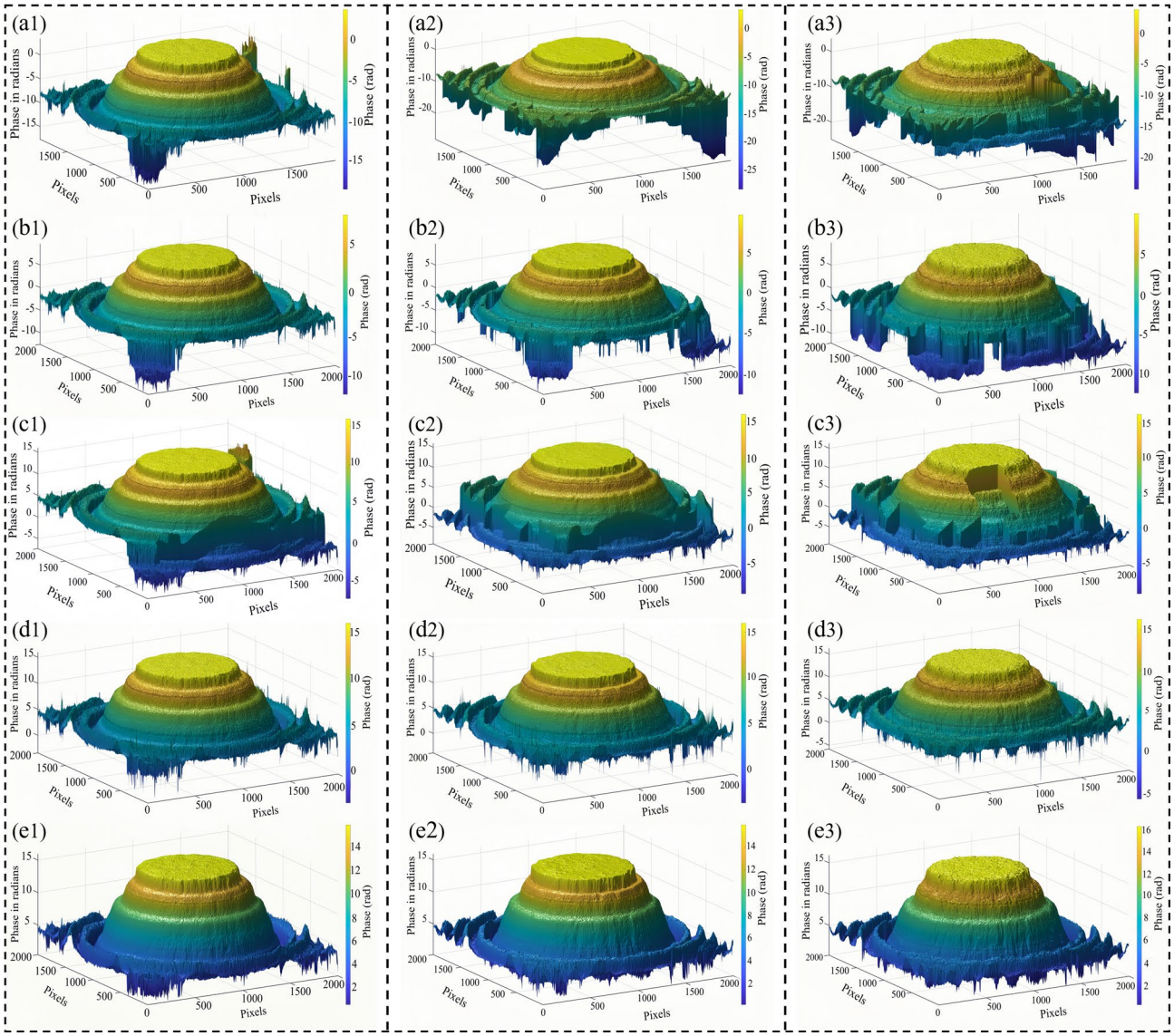

Fig. 15. Comparison of phase-distribution results obtained using five phase-unwrapping algorithms on three-frame transient interferometric images: Columns 1, 2, and 3 correspond to phase reconstruction results for frames 1, 2, and 3, respectively; Rows (**a**), (**b**), (**c**), (**d**), and (**e**) show the unfolded results from different algorithms: (a1), (a2), (a3) represent the Goldstein algorithm; (b1), (b2), (b3) represent the TIE algorithm; (c1), (c2), (c3) represent the N-F algorithm; (d1), (d2), (d3) represent the SRNCP algorithm; (e1), (e2), (e3) represent the improved algorithm.

In terms of phase smoothness, the improved algorithm yields values of 0.0902, 0.0735, and 0.0991, respectively, which are the lowest among all methods with only slight numerical variation, demonstrating better phase continuity and stronger noise suppression ability.

In addition, the number of unwrapping error regions counts the pixels or regions with phase discontinuities or abnormal jumps, thereby reflecting local distortion and error propagation; for this metric, lower values correspond to better performance. The improved algorithm produces only 451, 1007, and 1606 error regions, respectively, which are significantly fewer than those of the other methods. Its advantage is particularly evident compared with the Goldstein method, which exhibits the highest error concentration. These results further verify that the improved algorithm has stronger fault tolerance and robustness when dealing with phase jumps, high-gradient areas, and locally discontinuous regions.

In summary, the improved algorithm demonstrates optimal performance across all three core evaluation metrics, fully confirming its high precision and robustness in phase unwrapping.

Accuracy verification and evaluation in oil-film thickness reconstruction

After obtaining the continuous phase map, this section conducts a systematic evaluation of the improved algorithm's film-thickness reconstruction accuracy and engineering applicability under EHL conditions. The

Algorithm	Image frame number	Effective unwrapped Area (%)	Phase smoothness (GMSD)	Number of unwrapping error regions (pixel)
Goldstein Method	1	97.254	0.4647	10,287
	2	97.295	0.9947	20,305
	3	97.197	0.6447	22,694
TIE Method	1	97.631	0.0938	826
	2	98.100	0.1517	3345
	3	97.971	0.1812	5329
N-F Method	1	97.521	0.1415	3096
	2	97.987	0.1759	5631
	3	97.886	0.1875	6490
SRNCP Method	1	97.641	0.0923	798
	2	98.203	0.1077	1880
	3	98.150	0.1229	2716
Improved Method	1	98.642	0.0902	451
	2	98.906	0.0735	1007
	3	98.951	0.0991	1606

Table 4. Quantitative performance comparison of five phase-unwrapping algorithms across different evaluation metrics.

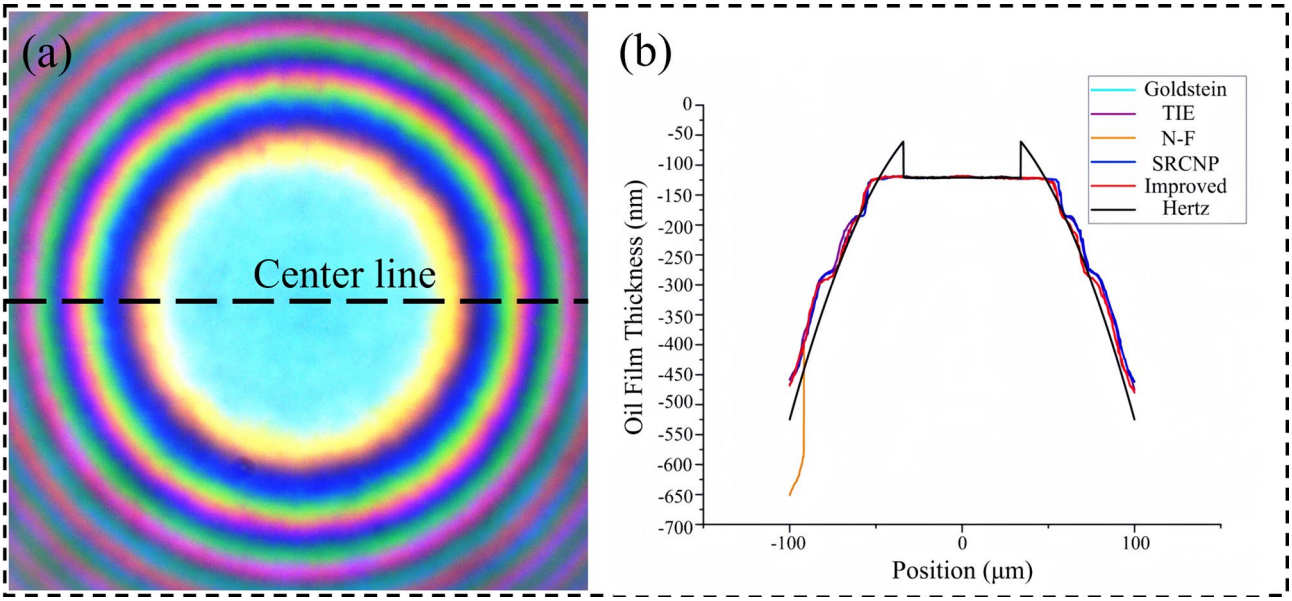

Fig. 16. Interference fringe pattern and comparison of reconstructed film thickness with theoretical model: (**a**) Interference fringe pattern and centerline position schematic; (**b**) Comparison of film thickness distributions reconstructed by five phase unwrapping algorithms with the Hertz theory model.

assessment is carried out through targeted experiments and quantitative metrics in three aspects: the consistency between the reconstructed oil-film thickness and the theoretical model, the profile reconstruction accuracy in the central contact region, and the algorithm's ability to recover the maximum oil-film thickness under dynamic conditions[39,43,44].

Consistency between oil film thickness and theoretical model thickness

To evaluate the accuracy of different phase unwrapping algorithms in reconstructing lubrication film thickness, this section utilizes interferometric measurement data collected under a 1 N load and 10 r/min rotational speed. The thickness distributions reconstructed by each algorithm are compared with those derived from the Hertz contact theory model. According to Hertz's theory, the contact gap between the steel ball and the glass plate can be calculated using an analytical formula[39]. However, since the model assumes an ideal abrupt transition at the contact boundary, whereas actual interference patterns typically exhibit smoother phase variations in this region, the theoretical curve shows local deviations from experimental results at the edge positions.

Figure 16(b) shows the comparison between the center-line film-thickness profiles reconstructed by different algorithms and the theoretical curve. It can be seen that the reconstructed curves of all algorithms exhibit high

Algorithm	RMSE (nm)	R^2
Goldstein Method	21.8891	0.9568
TIE Method	22.0177	0.9563
N-F Method	32.2131	0.9022
SRNCP Method	21.7940	0.9570
Improved Method	16.8805	0.9758

Table 5. Comparison table of five phase unwrapping algorithms with hertz model in EHL film thickness reconstruction.

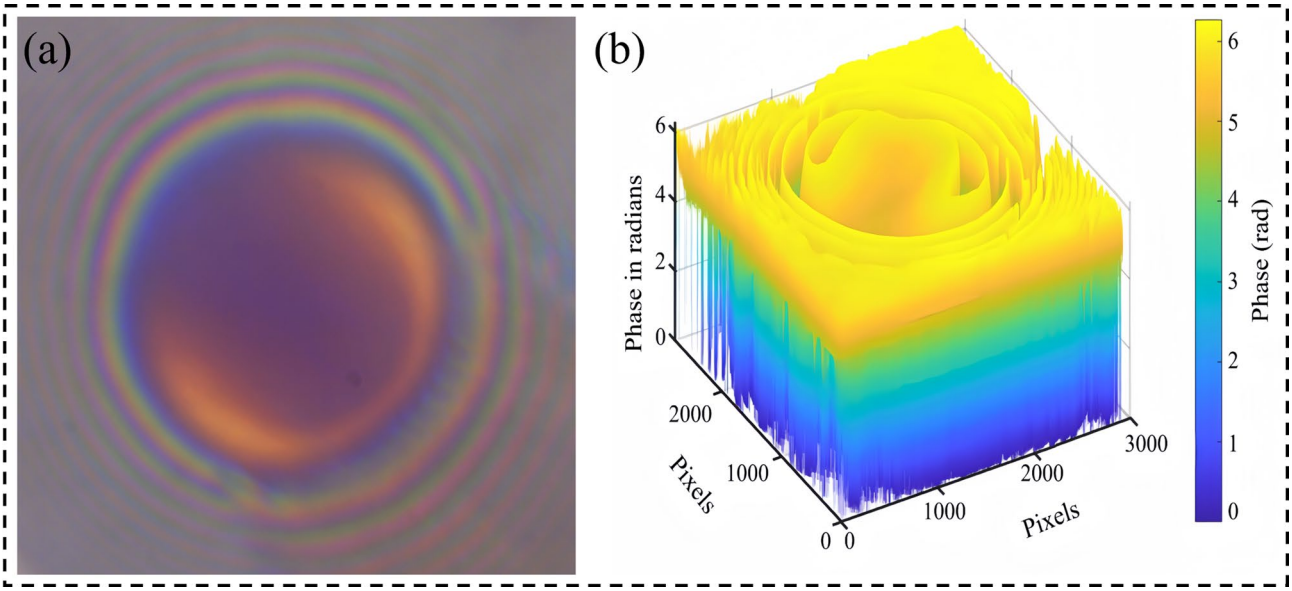

Fig. 17. Transient interference image and corresponding wrapped phase map: (**a**) Transient interference image (**b**) Wrapped phase map.

consistency with the Hertz model in the central contact region, while certain deviations appear in the boundary transition region due to the idealized assumptions of the theoretical model and imaging errors. In comparison, the improved algorithm is able to recover a more continuous and physically reasonable film-thickness variation in the edge region, and its reconstruction results show higher consistency with the interference-fringe patterns in Fig. 16(a).

To assess the reconstruction accuracy of each algorithm in practical film-thickness measurement, Root Mean Square Error (RMSE) and the coefficient of determination (R^2) are employed as quantitative evaluation metrics, as summarized in Table 5. RMSE characterizes the overall deviation of the reconstructed thickness from the reference result and reflects the global reconstruction error, with lower values indicating better performance. By contrast, R^2 evaluates the agreement between the reconstructed and reference results, thereby reflecting the goodness of fit of the thickness trend, where higher values correspond to better performance. The proposed method achieves the lowest RMSE (16.8805 nm) and the highest R^2 (0.9758), demonstrating that it yields the smallest reconstruction error and the best fitting consistency among all compared algorithms. This confirms the superiority of the improved algorithm in terms of both reconstruction accuracy and trend fidelity in film-thickness reconstruction.

Accuracy of the profile in the contact center area

To further verify the morphology reconstruction capability of the improved phase-unwrapping algorithm under dynamic conditions, this section uses transient interference images collected under a relative rotation of 30 r/min between the steel ball and glass disk, an experimental temperature of 20 °C, and a load of 15 N as the test samples. The algorithm's profile reconstruction accuracy in the central region of the oil film under transient conditions is then evaluated. Figure 17(a) shows the transient interference image acquired experimentally. Figure 17(b) displays the wrapped phase map extracted from it.

Figure 18 displays the 3D thickness profiles reconstructed for the central EHL oil film region under dynamic operating conditions using the Goldstein, TIE, N-F, SRNCP, and improved algorithms. It can be observed that the Goldstein and TIE algorithms exhibit significant thickness elevation and morphological distortion near the boundary regions, with poor axial symmetry. This indicates that their reconstruction results are affected by phase jump errors. The original SRNCP algorithm preserves relatively complete morphological features in

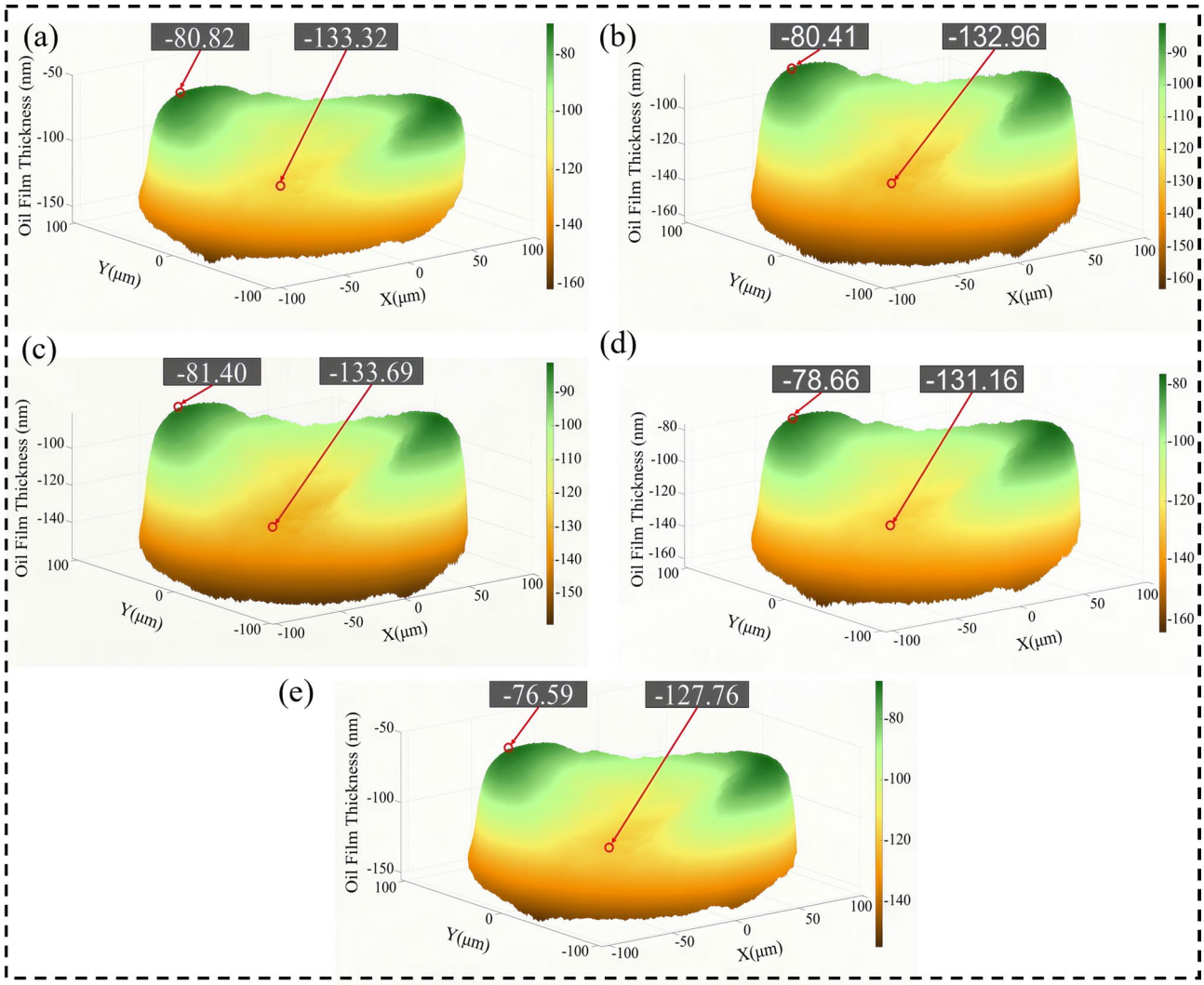

Fig. 18. Profile thickness maps of the oil-film central contact region reconstructed by five phase-unwrapping algorithms: (**a**) Goldstein algorithm; (**b**) TIE algorithm; (**c**) N-F algorithm; (**d**) SRNCP algorithm; (**e**) Improved algorithm.

Algorithm	Minimum central thickness (nm)	Maximum central thickness (nm)	Thickness range (nm)
Goldstein Method	80.82	133.32	52.50
TIE Method	80.41	132.96	52.55
N-F Method	81.40	133.69	52.55
SRNCP Method	78.66	131.16	52.55
Improved Method	76.59	127.76	51.17

Table 6. Comparison of extreme values in lubricating oil film thickness at the center region under five phase-unwrapping algorithms.

the central region, but local undulations persist at transition boundaries, compromising overall continuity. In comparison, the improved algorithm achieves a smoother, more symmetrical reconstruction of the central film profile, with no visible anomalies at the edges.

To quantify performance metrics, this study selected the thickness range within each reconstruction result as the comparative indicator. Table 6 summarizes the minimum and maximum film thickness values obtained by each algorithm in the central region under specified operating conditions. The results show that the minimum thickness reconstructed by the improved algorithm is 76.59 nm, with a maximum thickness of 127.76 nm. Its thickness range is more convergent compared to other algorithms, reflecting a more stable and physically reasonable film thickness recovery capability.

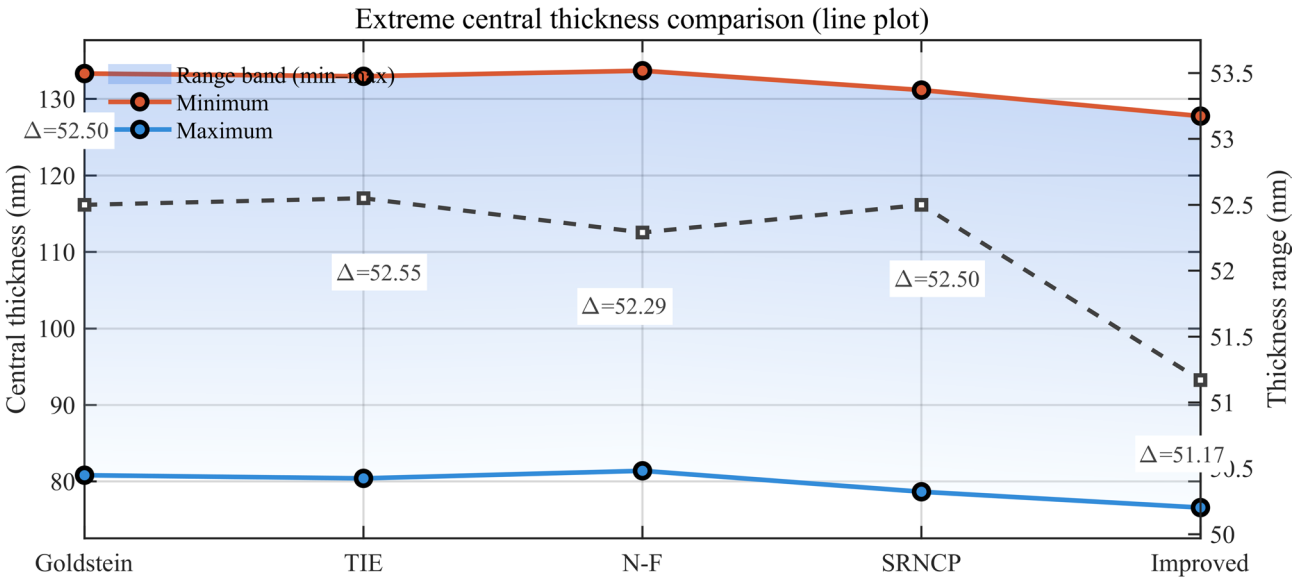

Fig. 19. Comparison of center film thickness extremes among five phase unwrapping algorithms.

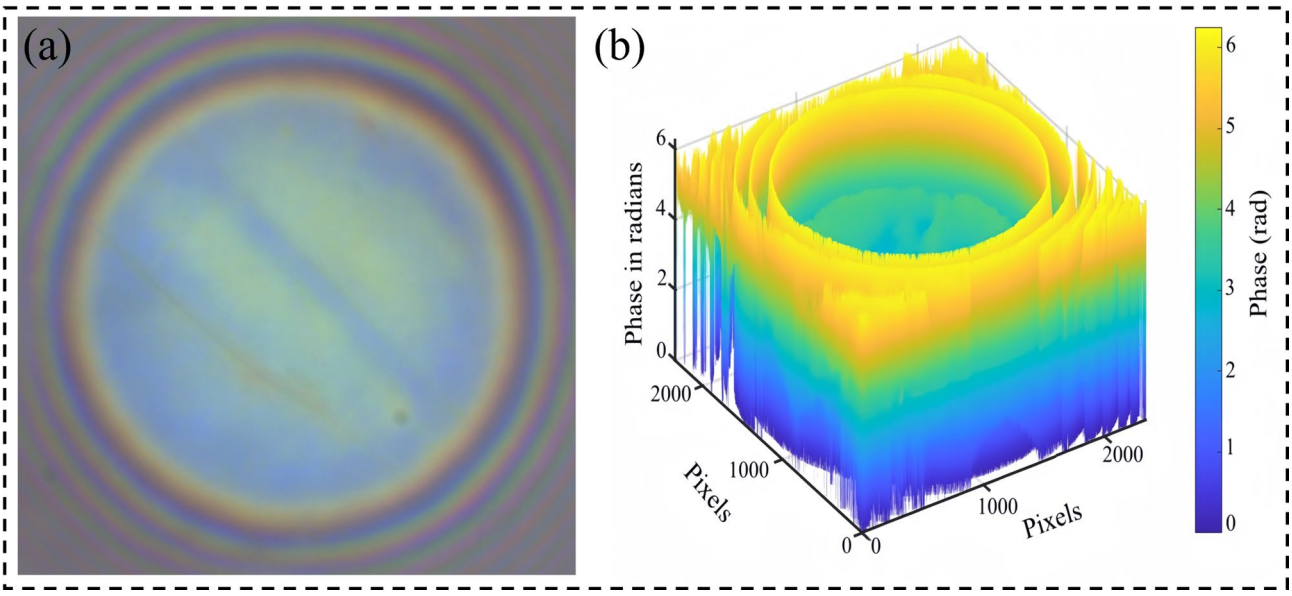

Fig. 20. Transient interference image and corresponding wrapped phase map: (**a**) Transient interference image (**b**) Wrapped phase map.

For a more intuitive comparison of these extreme values and their variation trends, Fig. 19 visualizes the data in Table 6 using a line plot.

Maximum oil film thickness recovery capacity assessment

To further validate the enhanced phase unwrapping algorithm's capability to recover maximum oil film thickness under dynamic operating conditions, this section evaluates the algorithm's film thickness reconstruction performance during transient states. Transient interferometric images collected from a steel ball rotating relative to a glass disc at 10 r/min, with an experimental temperature of 20 °C and a load of 5 N, were selected as test subjects. Figure 20 shows the experimentally acquired transient interference image. Figure 20(b) displays the phase unwrapping map extracted from it.

Figure 21 presents the 3D thickness reconstruction results obtained by each algorithm. It can be seen that the improved algorithm produces a clear oil-film profile with good axial symmetry and smooth thickness transitions, which is highly consistent with the expected trend of Hertzian contact theory. In contrast, the Goldstein, TIE, and N-F algorithms exhibit significant phase-jump errors and cumulative thickness distortions in the boundary

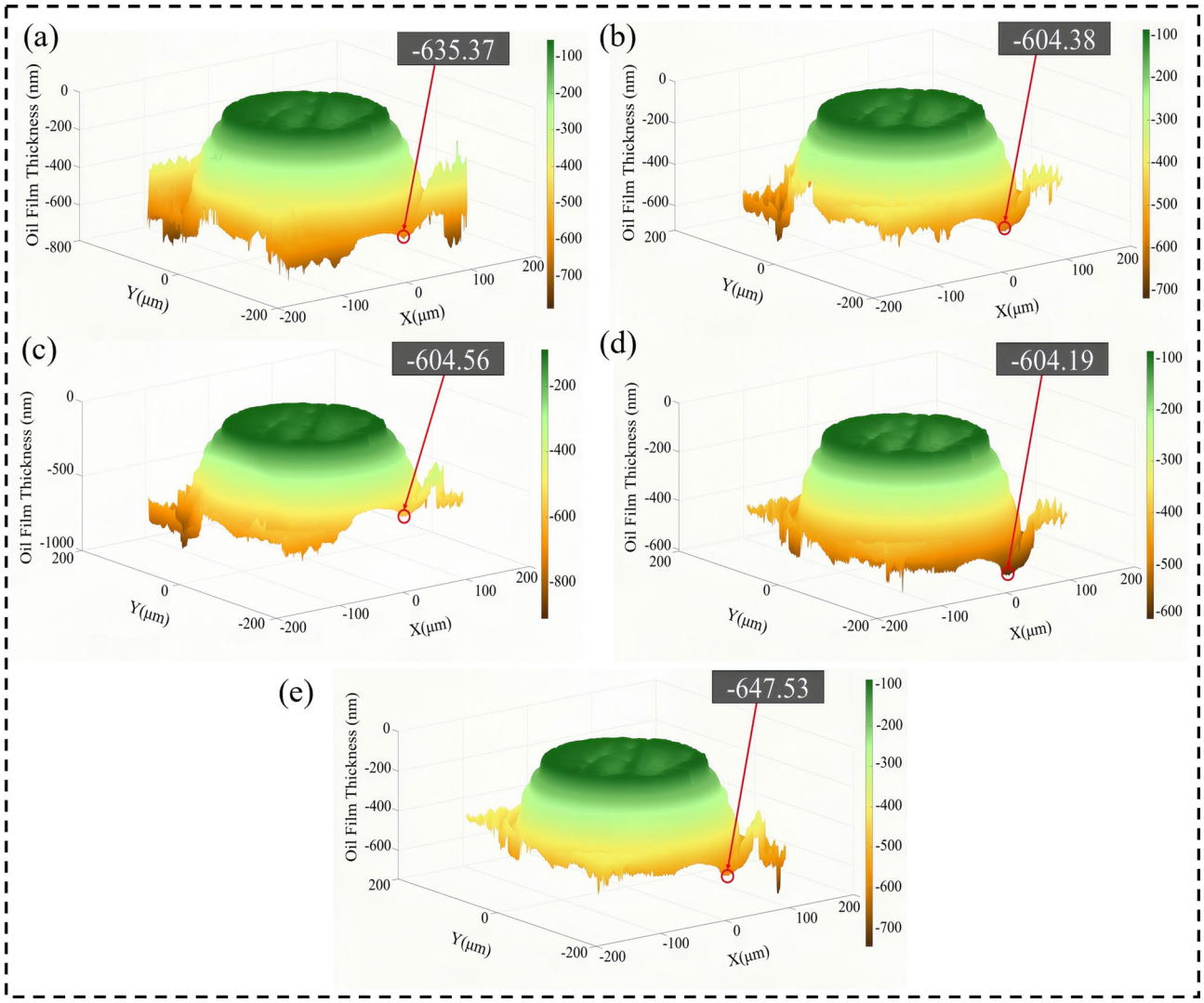

Fig. 21. Comparative map of the maximum oil-film thickness distributions reconstructed by the five phase-unwrapping algorithms: (**a**) Goldstein algorithm; (**b**) TIE algorithm; (**c**) N-F algorithm; (**d**) SRNCP algorithm; (**e**) Improved algorithm.

Algorithm	Maximum film thickness (nm)
Goldstein Method	635.37
TIE Method	604.38
N-F Method	604.56
SRNCP Method	604.19
Improved Method	647.53

Table 7. Comparison of the maximum lubricating oil-film thickness achieved by the five phase-unwrapping algorithms.

regions, resulting in noticeable deformation of the overall morphology. Although the original SRNCP algorithm shows improved structural fidelity compared with these methods, it still falls short of the improved algorithm in terms of edge continuity and transition smoothness.

To quantify performance metrics, this study selected the maximum lubricating oil film thickness from each reconstruction result as the comparative indicator. Since the glass plate serves as the reference surface, the measured film thickness values are expressed as negative values, with their absolute values corresponding to the actual oil film thickness. Relevant results are detailed in Table 7. It can be observed that the improved algorithm achieved the highest reconstruction accuracy, with a maximum oil film thickness reaching 647.53 nm.

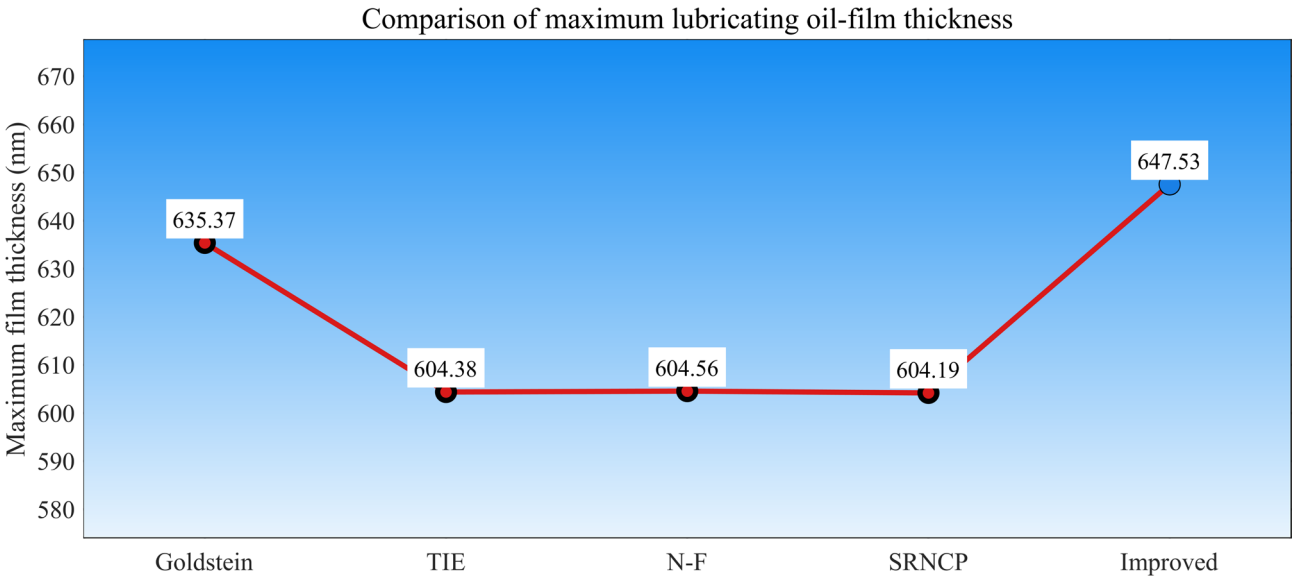

Fig. 22. Comparison of the maximum lubricating oil-film thickness.

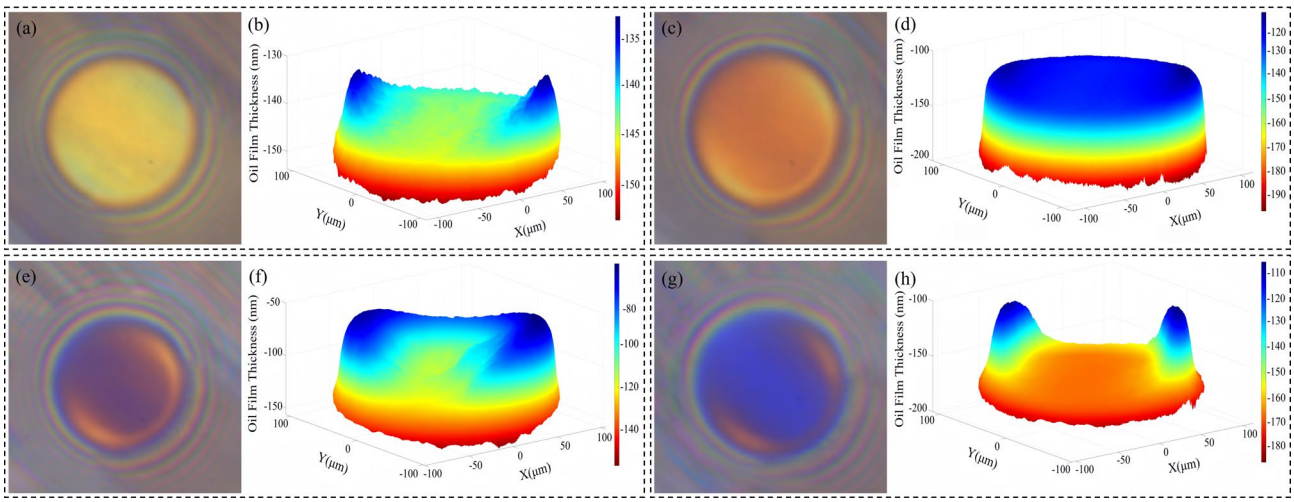

Fig. 23. Interference patterns at different rotational speeds and corresponding EHL film thickness distributions: (**a**) Interference pattern at 5 r/min; (**b**) Corresponding film thickness distribution; (**c**) Interference pattern at 10 r/min; (**d**) Corresponding film thickness distribution; (**e**) Interference pattern at 30 r/min; (**f**) Corresponding film thickness distribution; (**g**) Interference pattern at 45 r/min; (**h**) Corresponding film thickness distribution.

To facilitate an intuitive comparison of the maximum lubricating oil-film thickness achieved by different algorithms and their differences, Fig. 22 visualizes the data in Table 7 using a line plot.

Application of an improved phase unwrapping algorithm in EHL oil film thickness measurement

To validate the practical application effectiveness of the improved phase unwrapping algorithm in EHL oil film thickness measurement, transient interference images of the oil film were acquired under conditions of a constant normal load of 15 N and an ambient temperature of 20 °C. During the experiment, the relative rotational speed between the steel ball and glass disc was set to four operating conditions: 5, 10, 30 and 45 r/min, to evaluate the algorithm's reconstruction performance under different dynamic conditions.

As shown in Fig. 23, with increasing rotational speed, motion blur in the contact area progressively intensifies, and the contrast of interference fringes noticeably diminishes. This places higher demands on phase unwrapping and oil film thickness reconstruction. The improved phase unwrapping algorithm consistently achieves stable phase unwrapping under all the aforementioned operating conditions, yielding continuous, smooth three-dimensional oil film thickness distributions that align with contact characteristics. Figure 23 presents interference

images (a, c, e, g) acquired at different rotational speeds and their corresponding three-dimensional oil film thickness reconstructions (b, d, f, h). It can be observed that at 45 r/min, the reconstructed surface maintains a clear and coherent morphological structure, demonstrating the algorithm's robust performance against motion blur and reduced imaging contrast under dynamic EHL conditions.

Discussion on limitations

Under certain extreme conditions, this method may experience performance degradation or even failure. For instance: when fringe visibility is extremely low, hue phase extraction may become distorted; under severe undersampling conditions, insufficient spatial sampling density may cause the true phase increment between adjacent pixels to exceed the unique recovery threshold permitted by the principal value range (i.e., the absolute value of adjacent phase differences no longer remains less than π). In such cases, the observed unwrapped phase difference cannot be uniquely mapped back to the true phase difference. Consequently, the algorithm cannot correctly determine the number of 2π cycles to compensate, ultimately introducing unrecoverable phase ambiguity and causing unwrapping failure. Additionally, under conditions of excessive speckle noise or significant motion blur, local noise estimation and reliability assessment may also produce deviations, thereby affecting the stability and accuracy of the final unwrapping results.

Conclusion

This study addresses the issue that the SRNCP algorithm's reliability assessment in complex lubricating oil film interference images is susceptible to degradation from local noise and fringe degradation. It proposes an improved two-dimensional phase unwrapping method tailored for EHL measurement scenarios. By integrating phase gradient analysis with local noise estimation, this method enhances the reliability map construction and path guidance process within the SRNCP framework. Consequently, it improves phase unwrapping stability and oil film thickness reconstruction accuracy under complex operating conditions. Experimental evaluations using multiple sets of transient interference images demonstrate that the improved algorithm outperforms typical methods such as Goldstein, TIE, network flow, and the original SRNCP in terms of phase smoothness, error suppression capability, effective unwrapping region coverage, and thickness reconstruction accuracy. Particularly under EHL conditions, this method achieves high-precision reconstruction of the complete three-dimensional oil film morphology and reliably captures peak film thickness at the contact center region. Comparative analysis with Hertzian contact theory further validates its outstanding physical consistency and numerical accuracy. Furthermore, experimental results demonstrate that the algorithm maintains excellent robustness under dynamic conditions. Even when fringe visibility decreases and imaging quality degrades, it consistently outputs stable, continuous, and symmetrical film thickness reconstruction results, highlighting its outstanding adaptability and application potential in complex operational environments.

Future research will focus on extending this algorithm to measurement scenarios involving non-ideal lubrication systems, high-speed contact interfaces, and complex surface topographies, thereby broadening its application potential in engineering metrology, interfacial tribology research, and in situ diagnostic fields.

Data availability

The datasets used and analysed during the current study are available from the corresponding author on reasonable request.

Received: 23 January 2026; Accepted: 13 March 2026
Published online: 31 March 2026

References

1. De Groot, P. J. A review of selected topics in interferometric optical metrology. *Rep. Prog. Phys.* **82** https://doi.org/10.1088/1361-6633/ab092d (2019). 056101.
2. Wang, Y., Xie, F., Ma, S. & Dong, L. Review of surface profile measurement techniques based on optical interferometry. *Opt. Lasers Eng.* **93**, 164–170. https://doi.org/10.1016/j.optlaseng.2017.02.004 (2017).
3. De Groot, P. Principles of interference microscopy for the measurement of surface topography. *Adv. Opt. Photonics* **7**, 1–65. https://doi.org/10.1364/AOP.7.000001 (2015).
4. Chatterjee, S. & Bhardwaj, R. A short review on optical interferometry techniques for characterization of a thin liquid film on a solid surface. *Sādhanā.* **48**, 30. https://doi.org/10.1007/s12046-023-02091-6 (2023).
5. Creath, K. V phase-measurement interferometry techniques. In Progress in optics, (Elsevier), pp. 349–393. (1988). https://doi.org/10.1016/S0079-6638(08)70178-1
6. Hu, C. & Popescu, G. Quantitative phase imaging: principles and applications. In Label-Free Super-Resolution Microscopy, (Springer), pp. 1–24. (2019). https://doi.org/10.1007/978-3-030-21722-8_1
7. Herráez, M. A., Burton, D. R., Lalor, M. J. & Gdeisat, M. A. Fast two-dimensional phase-unwrapping algorithm based on sorting by reliability following a noncontinuous path. *Appl. Opt.* **41**, 7437–7444. https://doi.org/10.1364/AO.41.007437 (2002).
8. Takeda, M., Ina, H. & Kobayashi, S. Fourier-transform method of fringe-pattern analysis for computer-based topography and interferometry. *J. Opt. Soc. Am.* **72**, 156–160. https://doi.org/10.1364/JOSA.72.000156 (1982).
9. Lianqing, Y. L. X. X. Z. & Yonghong, W. S. W. Review of electronic speckle pattern interferometry (ESPI) for three dimensional displacement measurement. Chinese journal of mechanical engineering *27*, 1. (2014). https://doi.org/10.3901/CJME.2014.01.001
10. Massonnet, D. et al. The displacement field of the Landers earthquake mapped by radar interferometry. nature *364*, 138–142. (1993). https://doi.org/10.1038/364138a0
11. Dymerska, B. et al. Phase unwrapping with a rapid opensource minimum spanning tree algorithm (ROMEO). Magnetic resonance in medicine **85**, 2294–2308. (2021). https://doi.org/10.1002/mrm.28563
12. Zhang, S. Recent progresses on real-time 3D shape measurement using digital fringe projection techniques. *Opt. Lasers Eng.* **48**, 149–158. https://doi.org/10.1016/j.optlaseng.2009.03.008 (2010).
13. Takeda, M. & Mutoh, K. Fourier transform profilometry for the automatic measurement of 3-D object shapes. *Appl. Opt.* **22**, 3977–3982. https://doi.org/10.1364/AO.22.003977 (1983).

14. Srinivasan, V., Liu, H.-C. & Halioua, M. Automated phase-measuring profilometry of 3-D diffuse objects. *Appl. Opt.* **23**, 3105–3108. https://doi.org/10.1364/AO.23.003105 (1984).
15. Takasaki, H. Moiré topography. *Appl. Opt.* **9**, 1467–1472. https://doi.org/10.1364/AO.9.001467 (1970).
16. Li, C. et al. High precision computer-generated moiré profilometry. *Sci. Rep.* **9** https://doi.org/10.1038/s41598-019-44186-3 (2019). 7804.
17. Su, L., Su, X., Li, W. & Xiang, L. Application of modulation measurement profilometry to objects with surface holes. *Appl. Opt.* **38**, 1153–1158. https://doi.org/10.1364/AO.38.001153 (1999).
18. Wei, Z. et al. Dynamic phase-differencing profilometry with number-theoretical phase unwrapping and interleaved projection. *Opt. Express* **32**, 19578–19593. https://doi.org/10.1364/OE.527192 (2024).
19. Zheng, S. & Cao, Y. Fringe-projection profilometry based on two-dimensional empirical mode decomposition. *Appl. Opt.* **52**, 7648–7653. https://doi.org/10.1364/AO.52.007648 (2013).
20. Ghiglia, D. C. & Romero, L. A. Robust two-dimensional weighted and unweighted phase unwrapping that uses fast transforms and iterative methods. *J. Opt. Soc. Am. A* **11**, 107–117. https://doi.org/10.1364/JOSAA.11.000107 (1994).
21. Herszterg, I., Poggi, M. & Vidal, T. Two-dimensional phase unwrapping via balanced spanning forests. *INFORMS J. Comput.* **31**, 527–543. https://doi.org/10.1287/ijoc.2018.0832 (2019).
22. Zhao, M. et al. Quality-guided phase unwrapping technique: Comparison of quality maps and guiding strategies. *Appl. Opt.* **50**, 6214–6224. https://doi.org/10.1364/AO.50.006214 (2011).
23. Bioucas-Dias, J. M. & Valadao, G. Phase unwrapping via graph cuts. *IEEE Trans. Image Process.* **16**, 698–709. https://doi.org/10.1109/TIP.2006.888351 (2007).
24. Costantini, M. A novel phase unwrapping method based on network programming. *IEEE Trans. Geosci. Remote Sens.* **36**, 813–821. https://doi.org/10.1109/36.673674 (2002).
25. Wang, P. et al. A phase unwrapping method with the sparse prior for diffraction phase microscopy. *Opt. Laser Technol.* **170**, 110268. https://doi.org/10.1016/j.optlastec.2023.110268 (2024).
26. Hooper, A. & Zebker, H. A. Phase unwrapping in three dimensions with application to InSAR time series. *J. Opt. Soc. Am. A.* **24**, 2737–2747. https://doi.org/10.1364/JOSAA.24.002737 (2007).
27. Liu, F. & Pan, B. A new 3-D minimum cost flow phase unwrapping algorithm based on closure phase. *IEEE Trans. Geosci. Remote Sens.* **58**, 1857–1867. https://doi.org/10.1109/TGRS.2019.2949926 (2019).
28. Kajava, T., Lauranto, H. & Friberg, A. Interference pattern of the Fizeau interferometer. *J. Opt. Soc. Am. A.* **11**, 2045–2054. https://doi.org/10.1364/JOSAA.11.002045 (1994).
29. Cann, P., Spikes, H. & Hutchinson, J. The development of a spacer layer imaging method (SLIM) for mapping elastohydrodynamic contacts. *Tribol. Trans.* **39**, 915–921. https://doi.org/10.1080/10402009608983612 (1996).
30. Bruning, J. H. et al. Digital wavefront measuring interferometer for testing optical surfaces and lenses. *Appl. Opt.* **13**, 2693–2703. https://doi.org/10.1364/AO.13.002693 (1974).
31. Hariharan, P., Oreb, B. F. & Eiju, T. Digital phase-shifting interferometry: A simple error-compensating phase calculation algorithm. *Appl. Opt.* **26**, 2504–2506. https://doi.org/10.1364/AO.26.002504 (1987).
32. Hartl, M., Krupka, I. & Liska, M. Differential colorimetry: Tool for evaluation of chromatic interference pattern. *Opt. Eng.* **36**, 2384–2391. https://doi.org/10.1117/1.601415 (1997).
33. Ciulli, E., Draexl, T. & Stadler, K. Film Thickness Analysis for EHL Contacts under Steady-State and Transient Conditions by Automatic Digital Image Processing. Advances in tribology *2008*, (2008). https://doi.org/10.1155/2008/325187
34. Ciulli, E., Stadler, K. & Draexl, T. The influence of the slide-to-roll ratio on the friction coefficient and film thickness of EHD point contacts under steady state and transient conditions. *Tribol. Int.* **42**, 526–534. https://doi.org/10.1016/j.triboint.2008.04.005 (2009).
35. Arevalillo-Herráez, M., Villatoro, F. R. & Gdeisat, M. A. A robust and simple measure for quality-guided 2D phase unwrapping algorithms. *IEEE Trans. Image Process.* **25**, 2601–2609. https://doi.org/10.1109/TIP.2016.2551370 (2016).
36. Xie, X. et al. Deep learning phase-unwrapping method based on adaptive noise evaluation. *Appl. Opt.* **61**, 6861–6870. https://doi.org/10.1364/AO.464585 (2022).
37. Lu, Y., Zhao, W., Zhang, X., Xu, W. & Xu, G. Weighted-phase-gradient-based quality maps for two-dimensional quality-guided phase unwrapping. *Opt. Lasers Eng.* **50**, 1397–1404. https://doi.org/10.1016/j.optlaseng.2012.05.011 (2012).
38. Bonal, V. et al. Simultaneous determination of refractive index and thickness of submicron optical polymer films from transmission spectra. *Polymers* **13**, 2545. https://doi.org/10.3390/polym13152545 (2021).
39. Wheeler, J.-D. et al. A generalized differential colorimetric interferometry method: Extension to the film thickness measurement of any point contact geometry. *Tribol. Trans.* **61**, 648–660. https://doi.org/10.1080/10402004.2017.1386809 (2018).
40. Goldstein, R. M., Zebker, H. A. & Werner, C. L. Satellite radar interferometry: Two-dimensional phase unwrapping. *Radio Sci.* **23**, 713–720. https://doi.org/10.1029/RS023i004p00713 (1988).
41. Martinez-Carranza, J., Falaggis, K. & Kozacki, T. Fast and accurate phase-unwrapping algorithm based on the transport of intensity equation. *Appl. Opt.* **56**, 7079–7088 (2017).
42. Xue, W., Zhang, L., Mou, X. & Bovik, A. C. Gradient magnitude similarity deviation: A highly efficient perceptual image quality index. *IEEE Trans. Image Process.* **23**, 684–695. https://doi.org/10.1109/TIP.2013.2293423 (2013).
43. Marx, N., Guegan, J. & Spikes, H. A. Elastohydrodynamic film thickness of soft EHL contacts using optical interferometry. *Tribol. Int.* **99**, 267–277. https://doi.org/10.1016/j.triboint.2016.03.020 (2016).
44. Golafshan, R., Su, B., Jacobs, G. & Berroth, J. Characterization of elastohydrodynamic contact film thickness under high frequency force excitation using a 2D unwrapping-based image processing technique. *Tribol. Int.* **175**, 107841. https://doi.org/10.1016/j.triboint.2022.107841 (2022).

Acknowledgements

This work was supported in part by the Natural Science Foundation of Shanghai under Grant 25ZR1402180 and Chenguang Program of Shanghai Education Development Foundation and Shanghai Municipal Education Commission 25CGA57.Meanwhile, I sincerely thank the teachers and colleagues in the laboratory for their assistance and support throughout my research and studies.

Author contributions

L.X. conceived and designed the study, performed the experiments, analyzed the data, and wrote the original draft of the manuscript; Z.L. provided supervision and critical revision of the manuscript and served as the corresponding author; L.L. reviewed and edited the manuscript. All authors approved the final version of the manuscript.

Funding

This work was supported in part by the Natural Science Foundation of Shanghai under Grant 25ZR1402180 and Chenguang Program of Shanghai Education Development Foundation and Shanghai Municipal Education

Commission 25CGA57.

Declarations

Competing interests
The authors declare no competing interests.

Additional information
Correspondence and requests for materials should be addressed to Z.L.

Reprints and permissions information is available at www.nature.com/reprints.

Publisher's note Springer Nature remains neutral with regard to jurisdictional claims in published maps and institutional affiliations.